Tracing mantle-reacted fluids in magma-poor rifted margins: The example of Alpine Tethyan rifted margins.

V.H. Pinto,, Gianreto Manatschal, Anne Marie Karpoff, A. Viana

AGU PUBLICATIONS

Geochemistry, Geophysics, Geosystems

RESEARCH ARTICLE
10.1002/2015GC005830

Tracing mantle-reacted fluids in magma-poor rifted margins: The example of Alpine Tethyan rifted margins

Victor Hugo G. Pinto[1,2], Gianreto Manatschal[1], Anne Marie Karpoff[1], and Adriano Viana[3]

[1]Institut de Physique du Globe de Strasbourg, CNRS UMR7516, Université de Strasbourg, Strasbourg Cedex, France, [2]Petrobras S.A, E&P-EXP, Applied Geology to Exploration, Rio de Janeiro, Brazil, [3]Petrobras S.A, E&P-Libra, Exploration, Geology, Rio de Janeiro, Brazil

Key Points:
- Mantle-reacted fluids migrated through extensional detachment system
- Trace metals are good proxies for fluids flow in distal rifted margins
- Spatial-temporal model for fluids in Alpine Tethyan magma-poor rifted margins

Correspondence to:
Victor Hugo Pinto,
vpinto@unistra.fr

Citation:
Pinto, V. H. G., G. Manatschal, A. M. Karpoff, and A. Viana (2015), Tracing mantle-reacted fluids in magma-poor rifted margins: The example of Alpine Tethyan rifted margins, *Geochem. Geophys. Geosyst.*, *16*, 3271–3308, doi:10.1002/2015GC005830.

Received 27 MAR 2015
Accepted 8 AUG 2015
Accepted article online 12 AUG 2015
Published online 27 SEP 2015

Abstract The thinning of the crust and the exhumation of subcontinental mantle in magma-poor rifted margins is accompanied by a series of extensional detachment faults. We show that exhumation along these detachments is intimately related to migration of fluids leading to changes in mineralogy and chemistry of the mantle, crustal, and sedimentary rocks. Using field observation and analytical methods, we investigate the role of fluids in the fossil distal margins of the Alpine Tethys. Using Cr-Ni-V, Fe, and Mn as tracers, we show that fluids used detachment faults as pathways and interacted with the overlying crust and sediments. These observations allow us to discuss when, where, and how this interaction happened during the formation of the rifted margin. The results show that: (i) serpentinization of mantle rocks during their exhumation results in the depletion of elements and migration of *mantle-reacted fluids* that are channeled along active detachment system; (ii) in earlier-stages, these fluids affected the overlying syntectonic sediments by direct migration from the underlying detachments;(iii) in later-stages, these fluids arrived at the seafloor, were introduced into, or "polluted" the seawater and were absorbed by post tectonic sediments. We conclude that a significant amount of serpentinization occurred underneath the hyperextended continental crust, and that the mantle-reacted fluids might have modified the chemical composition of the sediments and seawater. We propose that the chemical signature of serpentinization related to mantle exhumation is recorded in the sediments and may serve as a proxy to date serpentinization and mantle exhumation at present-day magma-poor rifted margins.

1. Introduction

While many studies investigated fluid-rock interactions in thrust systems, subduction zones, and Mid-Ocean Ridges (MOR), only few focused in hyperextended rifted margins [*Manatschal*, 1999; *Manatschal et al*., 2000; *Engström et al*., 2007]. In particular the origin of fluids, when they form, how they interact with different reservoirs (mantle, crust, sedimentary basin, and seawater), and what are their migration pathways along distal rifted margins remain poorly understood.

Fluids can have different origins and their occurrence can be found in a wide range of extensional settings. In the Bohai basin in China, the occurrence of CO_2 and CH_4 accumulations in gas reservoirs has a characteristic mantle or magmatic signature given by C and He isotopes [*Jin et al*., 2004]. Nevertheless, the interplay of the widespread Cenozoic volcanism and the set of major normal faults [*Jin et al*., 2004] suggest that these gases were formed by magmatic activity and migrated through faults. In the southeast Brazilian rifted margins, CO_2 with a mantle signature is also recognized by isotopic composition of C and He [*Santos Neto et al*., 2011]. In the same margins, trace elements analyzed in petroleum accumulations in Cretaceous and Cenozoic reservoirs suggest a mantle source for those elements [*Szatmari et al*., 2011]. *Manatschal et al*. [2000] described an enrichment of likely mantle-derived trace elements in fault rocks from the Err detachment located in the most distal domain of the fossil Adriatic margin exposed in the Central Alps. In contrast, *Hayman* [2006] described how the introduction of aqueous species by infiltration of shallow meteoric fluids caused mineralogical changes along a western U.S. extensional detachment. In the Albian carbonate rocks from the Cantabrian basin, northern Spain, a strong signature of fluids enriched in Pb-Zn-Fe is described [*López-Horgue et al*., 2010; *Dewit et al*., 2012]. These hydrothermal systems occurred over hyperextended crust within a domain where magmatic rocks are found.

Some of the processes observed in hyperextended rifted margins may share many similarities with processes observed at oceanic domains. For example, hydrothermal vents along the Mid-Atlantic Ridge (MAR),

related to magmatic systems, expel fluids enriched in CO_2, H_2S, CH_4, and metals such as Cu, Zn, Fe, and Au [*Douville et al*., 2002; *Fouquet et al*., 2010; *Kelley and Shank*, 2010]. Hydrothermal vents related to serpentinization [*Kelley et al*., 2001] expel fluids enriched in H_2, CH_4, and Ca, Mg, Si, Fe, Mn, and Ni [*Delacour et al*., 2008; *Edmonds*, 2010; *Fouquet et al*., 2010; *Kelley and Shank*, 2010].

Sediments associated with mantle exhumation and/or magmatic systems in oceanic domains capture the signature of upwelling fluids, which can spread throughout long distances. These fluids can result in the transformation or neoformation of minerals, such as phyllosilicates, oxides, and carbonates recording the fluid composition and/or the modified seawater chemistry [*McKenzie et al*., 1990; *Buatier et al*., 1995]. Recently, *Saito et al*. [2013] presented a profile across the South Atlantic ocean from the Brazilian margin to the Namibia platform showing a Fe-Mn plume that extends over more than 3000 km. They highlight that the amount of Fe-Mn is much higher at slow-spreading systems than in fast-spreading systems, therefore serpentinization is probably one of the major processes controlling the release of Fe-Mn. This is supported by observation of Fe and Mn-rich hydrothermal vents related to serpentinization in the Saldanha field in the South Atlantic [*Dias et al*., 2011]. In this field, low-temperature fluids escape from centimetric vent orifices that are broadly distributed. Fe and Mn oxyhydroxides precipitate from the seawater due to the cooling and gradually more oxidizing conditions and are easily trapped in the contemporaneous sediments [*Dias et al*., 2011].

It has also been shown at slow-spreading systems and Ocean Continent Transitions (OCT) that serpentinization is intimately related to extensional detachment faults [*Picazo et al*., 2013; *Rouméjon and Cannat*, 2014 and references therein] and that fluids related to these tectonic settings have a characteristic signature [*Edmonds*, 2010]. Detachment faults similar to those recognized in oceans [*deMartin et al*., 2007; *Reston and Ranero*, 2011; *Picazo*, 2012; *Whitney et al*., 2013] have been described in the continental crust of rifted margins [*Froitzheim and Eberli*, 1990; *Manatschal et al*., 2001]. In these settings, fluid circulation seems to be related to extensional events and they are responsible for the alteration of basement rocks leading to retrograde metamorphic reactions [*Manatschal et al*., 2000].

This study focuses on the well-preserved rift-related Err detachment system exposed in the Lower Austroalpine and Penninic nappes in the Alps in SE Switzerland. This detachment system is responsible for the final exhumation of mantle rocks to the seafloor. Along the detachment system, a series of water-assisted retrograde metamorphic reactions associated with hydrothermal circulation can be observed. Serpentinization is one of these reactions, which resulted in the leaching of elements (e.g., Ni, Cr, V, Fe, and Mn) and the enrichment of fluids that posteriorly migrated along detachment faults into the overlying sedimentary basin. The occurrence of elements, derived from the mantle, in the fault rocks of the Err detachment and the overlying sediments enables us to link it to serpentinization and mantle exhumation during the final rifting. The aim of this paper is to investigate how and when these mantle-reacted fluids formed and migrated along the extensional detachment faults, and how they affected the crust and overlying sediments and seawater. We will also show that the imprint of mantle-reacted fluids can only be observed in the most distal margins along the final fault system associated with mantle exhumation, while earlier fault systems, located further inboard (more proximal) do not show this signature.

2. The Alpine Tethyan Margins

2.1. Rift Domains and Rift Evolution

Remnants of the Mesozoic Alpine Tethyan margins were recognized and described in the Alps. Their different paleogeographic domains (Figure 1) were defined based on the stratigraphic record [*Trümpy*, 1975; *Lemoine et al*., 1986; *Lemoine and Trümpy*, 1987]. More recently, *Mohn et al*. [2010, 2012] proposed the following subdivision:

(i) a proximal domain developed over an isostatically compensated continental crust characterized by grabens and half-grabens on a 25 km thick crust, (ii) a necking domain corresponding to a transitional zone between a little extended ($>$25 km) and a highly extended (or thinned) continental crust ($<$10 km), (iii) a highly thinned ($\sim$10 km), brittle continental crust characterized by extensional detachment faults and supradetachment basins, (iv) a zone of exhumed continental mantle grading into (v) an embryonic oceanic domain.

Each of these rift domains shows a complex time/space evolution resulting in a complex 3-D rift architecture. Despite the Alpine overprint, the local preservation of remnants of the former rifted margins enables

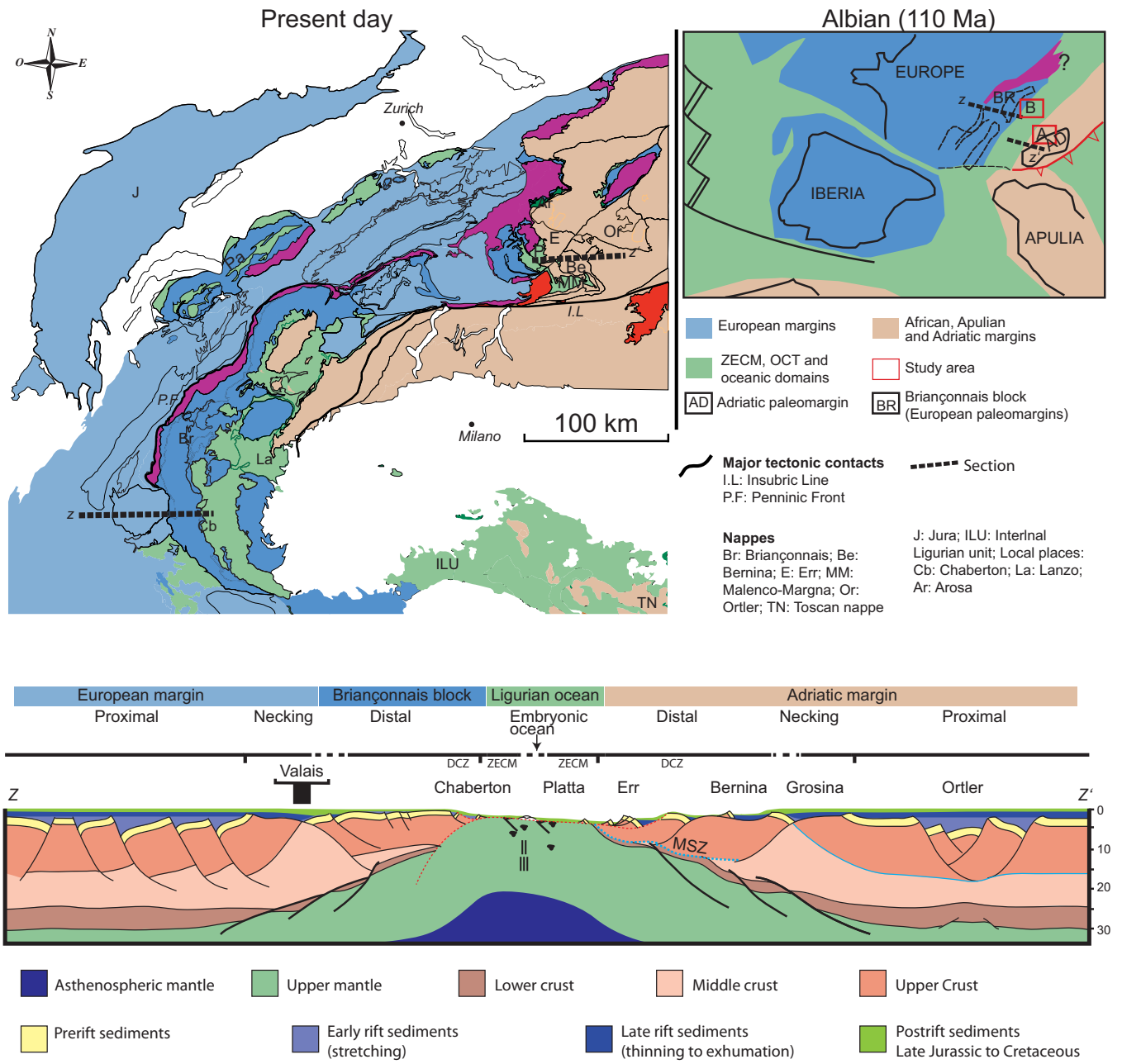

Figure 1. Tectonic and paleogeographic maps, and cross section through the former Alpine Tethyan margins. The present-day tectonic map (modified from *Schmid et al*. [2004] and *Mohn et al*. [2010]) shows a simplified subdivision of the main domains of the Alpine Tethyan margins. The paleogeographic map shows the continent and margin position at the Albian times. Red squares in the paleogeographic map are the position of the studied areas in Adriatic margin (A) and the Briançonnais (B). The composite cross-section through the conjugate margins of Adria and Europe/Briançonnais in a direction that the Valais domain is not present. The domains in the distal margin are referred as the Zone of Exhumed Continental Mantle (ZECM) and Distal Continental Zone (DCZ). Dotted blue line is the Margna shear zone (MSZ).

the recognition of the rift-related structures and their relation to basement and sedimentary rocks [e.g., *Manatschal*, 2004]. This allowed the definition of different rift stages that include: (i) an early Hettangian to Sinemurian rift event (stretching phase) linked to fault bounded basins filled by carbonate-bearing debris flows and turbidites interleaved with hemipelagic sediments, and sealed by marls and limestones dated as Pliensbachian/Toarcian [*Lemoine et al*., 1986; *Eberli*, 1988]; (ii) a late rift event (thinning and exhumation phases) that affected the future distal part of the margin; and (iii) an embryonic oceanic stage.

Müntener et al. [2000] and *Mohn et al*. [2012] showed that in the lower Austroalpine nappes, upper crustal rocks are locally juxtaposed against lower crustal rocks along a pre-Alpine shear zone (e.g., Margna shear

zone). They suggested that the major crustal thinning was accommodated along this shear zone in the middle crust that thinned the crust to about 10km (Figure 1). These authors also demonstrated with thermochronological data that the thinning/necking of the continental crust had to occur at about 190–185 Ma. Furthermore, *Desmurs et al*. [2001] showed that when the Err detachment fault penetrated the mantle and initiated mantle exhumation, the crust was already thinned to about 10km. The latter event, resulting in the formation of the most distal margin, is well recorded in the Lower Austroalpine Err nappe and in the Upper Penninic Platta nappe in Grisons in southeastern Switzerland (Figure 2) [*Manatschal*, 1995; *Froitzheim and Manatschal*, 1996; *Desmurs et al*., 2001; *Masini et al*., 2011] and will be described in the following chapter.

2.2. The Continental Distal Zone (CDZ) and the Zone of Exhumed Continental Mantle (ZECM) Exposed in the Err and Platta Nappes

Despite the Alpine deformation, remnants of the fossil Adriatic distal margin are well preserved in the Err and Platta nappes. The metamorphic overprint in basement rocks from these nappes did not exceed 350°C and the sediments of these units show in its northern part diagenetic to anchizonal conditions [*Trommsdorff and Evans*, 1974; *Manatschal*, 1995; *Ferreiro Mählmann*, 1996]. The fact that the basement and sedimentary rocks are locally only weakly affected by Alpine overprint enables the recognition of Jurassic rift structures and their contacts with sediments and basement. This makes the Err and Platta nappes one of the best examples world-wide to study the structural and stratigraphic evolution of a magma-poor rifted margin. Therefore, we used these sites to investigate the tectonic and fluid circulation history associated with the final stage of rifting and mantle exhumation in a magma-poor rifted margin.

The remnants of the former distal margin exposed in the Err and Platta nappes can be considered as analogues of present-day magma-poor distal rifted margins [*Péron-Pinvidic and Manatschal*, 2009; *Sutra and Manatschal*, 2012]. The reconstruction of these nappes shows a former distal margin with at least 50km in transport direction [*Manatschal*, 1995; *Manatschal and Nievergelt*, 1997; *Desmurs et al*., 2001; *Masini et al*., 2012]. The distal margin (Figure 2) can be subdivided into two subdomains: the Continental Distal Zone (CDZ; e.g., Err nappe) and the Zone of Exhumed Subcontinental Mantle (ZECM; e.g., Platta nappe). Both zones are formed by the same extensional Err detachment system that is Early to Middle Jurassic in age as indicated by its relationship with the syn and post tectonic sediments and magmatic systems [see *Eberli*, 1988; *Desmurs et al*., 2001; *Masini et al*., 2011 for more details].

The remnants of the ZECM are characterized by subcontinental serpentinized lherzolites with local occurrences of dunites and pyroxenites [*Desmurs et al*., 2001; *Müntener et al*., 2010]. The restoration of the Platta nappe enabled to define two units, referred to as the Upper and Lower Serpentinite Units (USU and LSU), representing, respectively, a more proximal and a more distal part of the ZECM [*Desmurs et al*., 2001; *Schaltegger et al*., 2002; *Müntener et al*., 2010]. While in the USU magmatic rocks are rare, in the LSU MORB-bearing magmatic rocks are observed and they testify the nature of the embryonic ocean [*Manatschal and Müntener*, 2009].

Key structures and metamorphic reactions observed in the ZECM, record the exhumation path of the mantle rocks to the seafloor. In the USU, pyroxenite dykes parallel to the high-temperature spinel foliation [*Desmurs et al*., 2001] indicate that they equilibrated in the spinel stability field [*Klemme*, 2004]. In the LSU, *Desmurs et al*. [2001] described the occurrence of high-temperature (600–700°C) hornblende around clinopyroxene. Hornblende growth was followed by a widespread hydration at lower temperature expressed by the crystallization of tremolite at the expense of clinopyroxene and Mg-hornblende. However, the hornblendes could not be dated and their relation to the Jurassic rifting cannot be demonstrated. In contrast, the serpentinization predates the Alpine compression and it is related to the Jurassic rifting [*Desmurs et al*., 2001; *Picazo et al*., 2013]. Serpentine often appears as a mesh-like structure and is associated with magnetite. Spinel is often altered to Cr-chlorite and magnetite, which marks a temperature between 200 and 300°C [*Klein et al*., 2013]. In general the serpentine minerals are partially replaced by calcite at or near seafloor, resulting in the so-called ophicalcites [*Bernoulli and Weissert*, 1985; *Picazo et al*., 2013]. Phlogopite Ar/Ar ages (160 $\pm$ 8Ma) from pyroxenite layers in the peridotites of other Penninic nappes close to the Platta are interpreted as cooling ages documenting mantle exhumation [*Peters and Stettler*, 1987; *Desmurs et al*., 2001].

Magmatic intrusive rocks also record a final deformation and mantle exhumation event, and some of the extrusive magmatic rocks postdate the extension. Most gabbros intruded into the already serpentinized

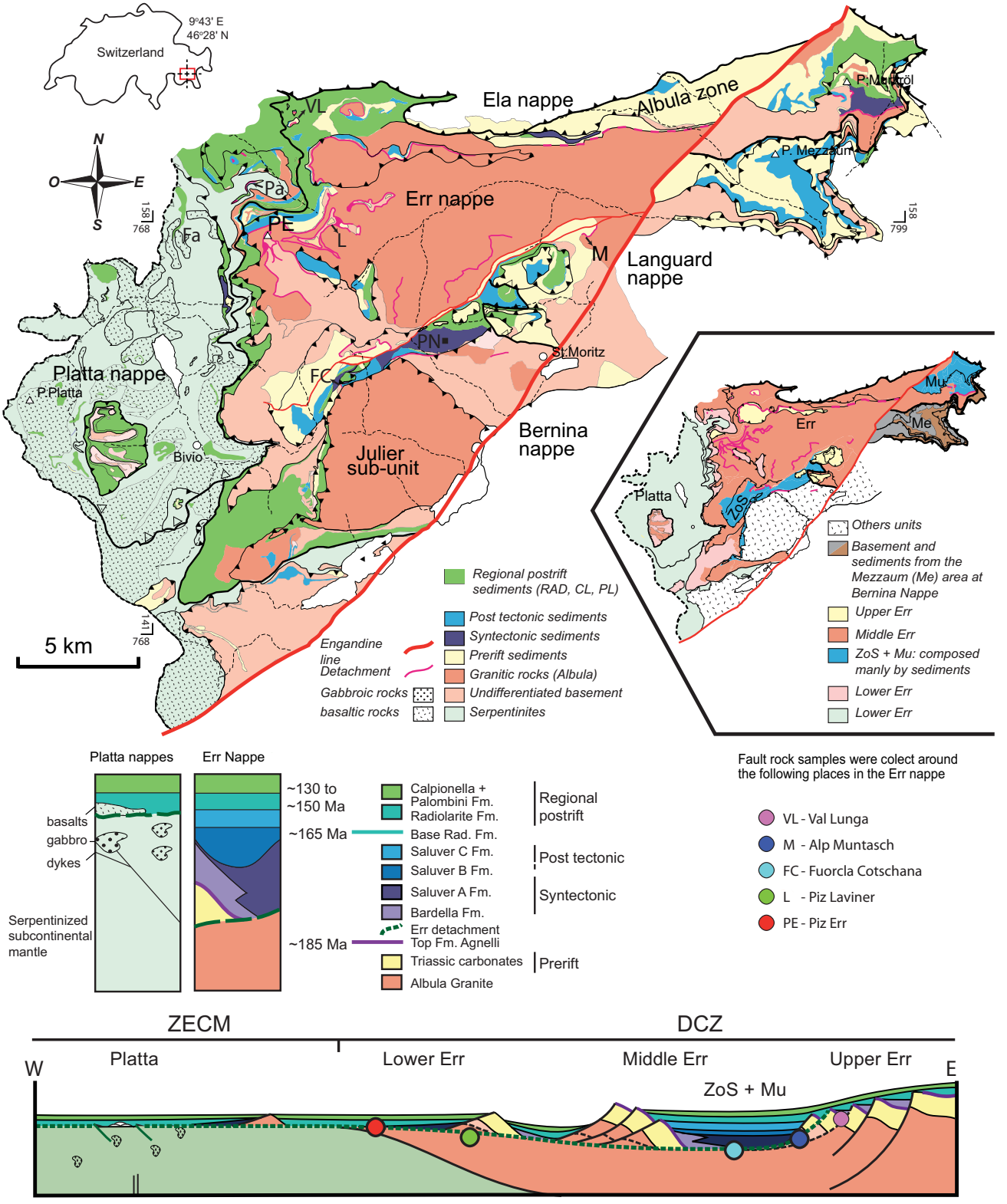

Figure 2. Tectonic map modified from *Mohn et al*. [2011] and cross section of the Err and Platta nappes. The Err nappe is part of the former DCZ and the Platta nappe is the former ZECM. Notice the distribution of the sedimentary sequences in the ZoS (Zone of Samedan) and Murtiröl (small tectonic map at right). Localities abbreviations are: Fa: Fallota, Pa: Parsettens, PN: Piz Nair, VL: Val Lunga; FC: Fuorcla Cotschana; M: Alp Muntatsch; Mu: Murtirol; and Me: Mezzaum. The cross section passes through the subunits of the Err and the Platta nappes (modified from *Masini et al*. [2012]). Colored dots represent the areas where samples were collected along the Err detachment fault (ED). The map is in Swiss grid (CH1903 in km).

mantle at shallow level at high to moderate temperatures at 161 ± 1Ma [*Desmurs et al*., 2001; *Schaltegger et al*., 2002].

2.3. The Syn to Post Tectonic Sedimentary Sequences in the Distal Margin

In the CDZ, the syn to post tectonic sedimentary sequences are developed in supradetachment basins [*Masini et al*., 2012] and they are different from those described in the proximal margin [*Mohn et al*., 2010; and references therein]. The sediments in the CDZ either overlie the Agnelli formation or are directly deposited over an exhumed basement and are sealed by the postrift Radiolarian cherts. The syn to post tectonic sequences are formed by the Bardella and Saluver formations, which were originally distinguished by their clasts composition and grain size [*Finger*, 1978]. *Masini et al*. [2011] subdivided the Bardella and the Saluver formations in three genetic sequences (basal, intermediate, and top-facies tracts) deposited in supradetachment basins with deposition controlled by the evolution of the Err detachment fault. The basal facies tract is made of the Bardella and Saluver A formations, the intermediate corresponds to the Saluver B formation, and the top facies tract is referred to as the Saluver C formation (Figure 2).

The Bardella and Saluver A formations were deposited during the onset of detachment faulting and early exhumation of the detachment footwall at the sea floor. Both formations correspond to sedimentary breccias and are proximal relative to theirs sources. The Saluver B is best characterized by turbidite sequences. The Saluver C contains interbedded shales and thin sandstone turbidites at the base, and predominantly shales at the top.

The Radiolarite formation overlies the Saluver C formation and is the first sedimentary sequence found over exhumed mantle and basalts in the ZECM. Therefore, it is referred to as the first regional postrift sediments. The Radiolarite formation is made of silica-rich radiolarian cherts and hydrothermal chert layers interbedded with thin reddish shales dated as Bathonian to Callovian [*Baumgartner*, 1987; *Cordey and Bailly*, 2007]. These sediments are overlain by the Tithonian to early Berriasian Calpionella Limestone formation (e.g., Aptychus Limestone from *Cornelius* [1932]), comprising micritic limestones and thin carbonaceous shales [*Bracciali et al*., 2007]. This sequence is overlain by early Berriasian to late Hauterivian-early Barremian Palombini shales [*Marroni et al*., 2000] composed of black shales and levels of marls. The youngest sequence in this domain is made of thin Cretaceous flysch sequences (Figure 2).

2.3.1. Time Markers and Correlation Levels

Two time markers (Figure 2) are essential to understand the evolution of the detachment system and of the supradetachment basin exposed in Err and Platta nappes [*Masini et al*., 2011]. The first corresponds to the *Top of Agnelli Formation* (TAF), dated at about 185Ma [*Dommergues et al*., 2012]. The Bardella and Saluver formations unconformably overlie the TAF. This gives a maximum age for these formations. The second time marker corresponds to the base of the *Radiolarite formation* (RAD), dated as 165Ma [*Bill et al*., 2001]. The Saluver and Bardella formations are unconformably overlain by the RAD. Thus, 165 Ma is a minimum age for these formations. The Radiolarite formation also lies above the serpentinites, basalts, and exhumed gabbros in the Platta nappe. Therefore, the RAD has to be Callovian (161Ma) or younger.

The observation that fault rocks of the Err detachment system can be found reworked in the Bardella and Saluver A formations [*Froitzheim and Eberli*, 1990; *Froitzheim and Manatschal*, 1996], and that rocks of the Agnelli Formation are truncated by the detachment fault, give maximum and minimum ages for the Err detachment that is between 185 and 165Ma. Since stratigraphic ages are rare in the CDZ, the ages used in this study are approximate ages for the activity of the Err detachment in the CDZ. Detachment faulting in the ZECM had to have lasted at least until 161Ma, corresponding to the onset of magmatic activity and deposition of radiolarian cherts.

2.4. Extensional Detachment Faults

2.4.1. Fault Rocks Related to Detachment Faults in the Mantle

Fault rocks related to extensional detachment faults in the serpentinized mantle in the ZECM (Platta nappe) are characterized by low-temperature brittle structures formed under similar conditions from those in the adjacent CDZ (Err nappe) [*Manatschal*, 1999]. They consist of foliated serpentinite cataclasites and gouges (Figure 3g). The foliated serpentinite cataclasites contain clasts of highly serpentinized peridotites and veins of serpentine and chlorite. Fractures, extensional veins, and open space filling veins (Figures 3i, 3j, and 3l) are common in these rocks. Gouges are made of rounded and sigmoidal clasts in a dark green matrix of serpentines, chlorite, and calcite. They often occur at the top of the fault zone and highlight the localization of deformation (Figures 3g and 3h). The gouges are overlain by tectonosedimentary breccias (~1.5m) consisting

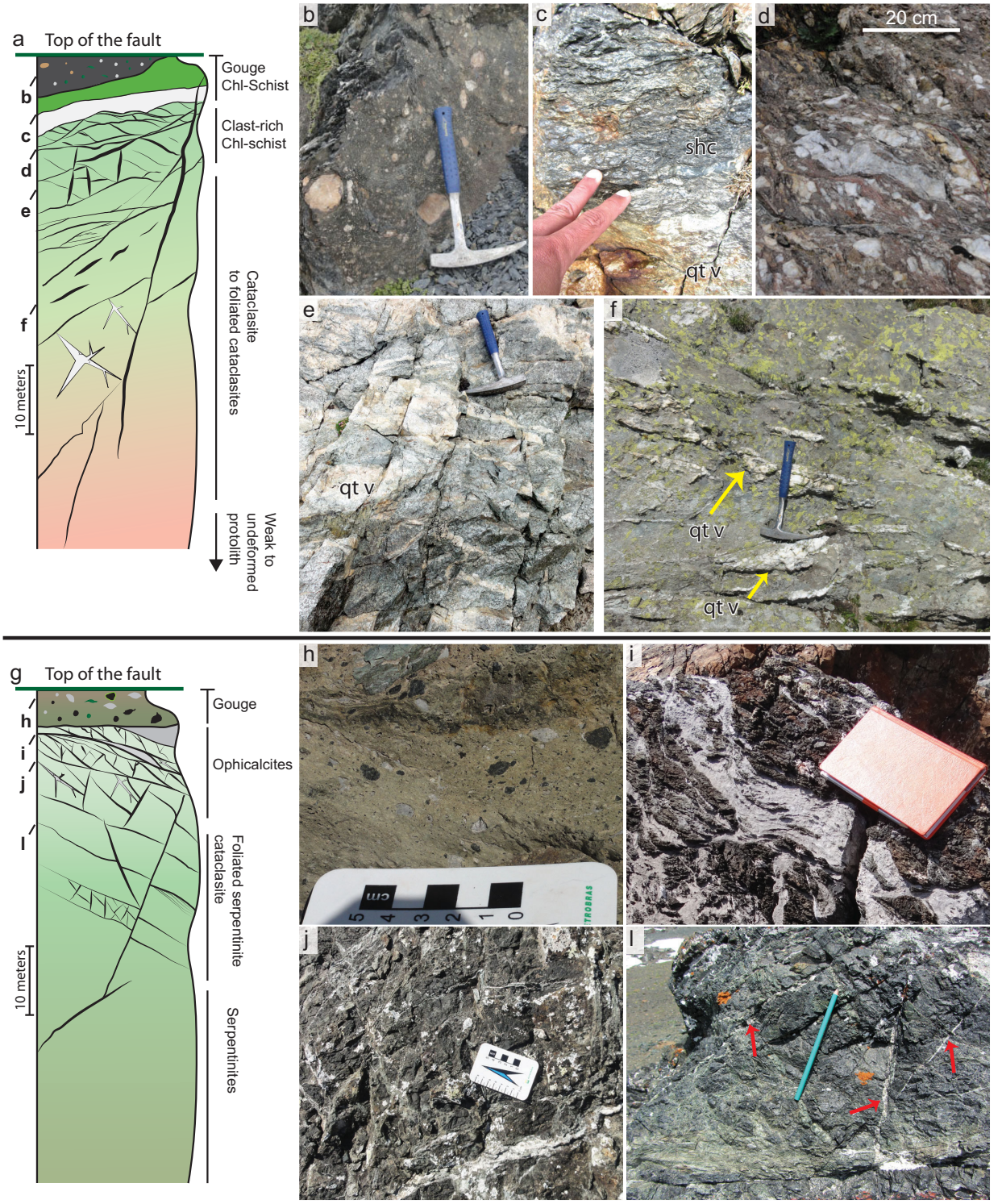

Figure 3. Extensional detachment fault profile and its main fault rocks in the exhumed mantle and in the continental crust. (a) Composite rock profile of detachment faults from Err, Bernina, Grosina, and Chaberton. Some of the rock types are absent in the mentioned detachments, but cataclasites are always observed. White polygons are the most prominent quartz veins and black lines are small secondary fault and fractures that, in most of the cases, are filled by quartz veins. (b) Black gouge with clast of Triassic dolomite. (c) Contact between chlorite-schist and tabular quartz vein (Grosina). (d) Clast-rich chlorite-schist (Fuorcla Cotschana) showing fractured quartz veins. (e) Foliated cataclasite and different sets of quartz veins (Fuorcla Cotschana). (f) Quartz veins parallel/subparallel to the foliation of cataclasites (Parsettens). (g) Rock profile from extensional detachment fault in the exhumed mantle at Platta nappe. Light gray polygons are main calcite veins. Black lines are small secondary fault and fractures that, in most of the cases, are filled by chlorite, serpentine, and calcite veins. (h) Gouges showing rounded clasts of serpentinites. (i) Ophicalcite with centimetric veins of calcite (light gray) parallel to the serpentinite foliation. (j) Ophicalcite with different orientations of calcite veins cutting serpentinites. (l) Calcite veins (red arrows) cutting previous serpentinite foliation intensely fractured. Ophicaltization is more prominent in Figure 3i compared to Figure 3l.

of clasts of reworked serpentinized peridotites within a serpentine-chlorite-calcite matrix that is often cut by millimetric calcite veins. Ophicalcites are commonly related to these fault rocks and consist of partially calcified serpentinites showing clasts of host-rock (serpentinites) cut by millimetric to centimetric calcite veins. Jigsaw clasts highlight an in situ deformation of the ophicalcites. The formation of ophicalcites implies an important fluid-rock interaction at a final stage of mantle exhumation at the seafloor (Figures 3i, 3j, and 3l) [*Bernoulli and Weissert*, 1985; *Picazo et al*., 2013]. The importance of fluid flow is also shown by crack-seal processes and the remarkable quantity of Fe-oxides (Figures 4d–4f). *Früh-Green et al*. [1990] analyzed similar calcite veins from the ophicalcites in the nearby Arosa unit. They determined a formation temperature lower than about 100°C interpreting that those veins formed at the presence of hydrothermal activity.

2.4.2. Fault Rocks Related to Detachment Faults in the Continental Crust

2.4.2.1. Macrostructural Observations

The fault rocks of the extensional Err detachment system mainly consist of green cataclasites and, to a lesser extent, black gouges (Figure 3a) [*Manatschal*, 1999]. The cataclasites contain a phyllosilicate-rich matrix of predominantly chlorite and sericite surrounding dispersed angular clasts, in places forming a well-defined foliation. The gouges (Figure 3b) contain millimetric to centimetric rounded clasts and a matrix of predominantly chlorite and illite. The gouges are found at the uppermost part of the fault zones, defining the localization of deformation.

Between these layers, two other characteristic rocks, not previously described, have been observed in the Err and in other Jurassic extensional detachment systems. The first one is a clast-rich chlorite-schist found above the foliated cataclasite. This rock-type has a typical schistosity but they have brecciated structure with abundant clasts, which allow us to differ them from foliated cataclasites. The second is a chlorite-schist where clasts are rare or absent. Chlorite-schist likely defines the localization of deformation. Field and thin section observations show that the fault-rock development was accompanied by retrograde metamorphic reactions that became more intense toward the fault core, i.e., increased from bottom to top. As shown in following sections, this reaction yields (i) a loss of SiO_2 resulting in the formation of quartz veins along the fault zone, and (ii) chlorite-rich layers.

Quartz veins are common along these extensional detachment systems and their width can range from meters to few millimeters. They usually appear parallel to subparallel to the fault rock foliation (Figure 3f), with tabular shape (Figure 3c) but also without preferred orientation. They can be cut by fractures and small-displacement faults (Figure 3e). Due to progressive cataclasis, quartz veins are often intensely fractured and deformed, and both angular and rounded clasts of vein material can be found in the fault rocks. The recognition of several generations of veins, some of which are brecciated, shows that veining is a multistage process.

In the Err detachment, the fault zone can vary in thickness from more than 100 m (Piz Laviner area) to about 20 m (Alp Muntatsch). Cataclasites and foliated cataclasites are widespread as well as gouges, but chlorite-schists can be absent. Along the Bernina detachment, the fault zone is up to 50m thick and is mainly composed of cataclasites. Gouges are rare and chlorite-schists were not observed. The Grosina detachment consists at least of two detachment faults. In our study, we investigated the lower one described by *Mohn et al*. [2011, 2012]. This detachment fault zone has up to 15 m of cataclasites. While gouges are not observed at its top, ultracataclasites and chlorite-schists are widespread. The brittle deformation affects a mylonitic zone of unknown age [*Mohn et al*., 2012]. Another, yet less explored example is the Chaberton detachment (see Figure 1 for location) belonging to a pre-Piemont units of the Western Alps, near Briançon. This detachment system is made of cataclasites, gouges, and chlorite schists.

2.4.2.2. Microstructures and Mineralogical Characteristics of the Fault Rocks

In order to evaluate the deformational and fluid-rock reaction histories of the detachments, the fault rocks were investigated using optical microscopic and powder X-ray diffraction (XRD) analyses.

The Albula granite, the protolith for most of the fault rocks along the Err detachment, has an original composition of 40%–60% plagioclase, 10%–30% K-feldspar, 25%–45% quartz, 5%–10% slightly chloritized biotite, and rare amphibole. The Albula granite was slightly altered and contains weakly chloritized biotite and sericite growth on K-Feldspar. It also contains fractures, some of which are filled by micrometric calcite veins. Apart from the fractures, no brittle structure (i.e., cataclastic flow) is observed in the Albula granite.

In the fault zone, the rocks are strongly altered by saussuritization processes, which we take to include all alteration processes of feldspar and other phases (e.g., chloritization of biotite) that result in the formation

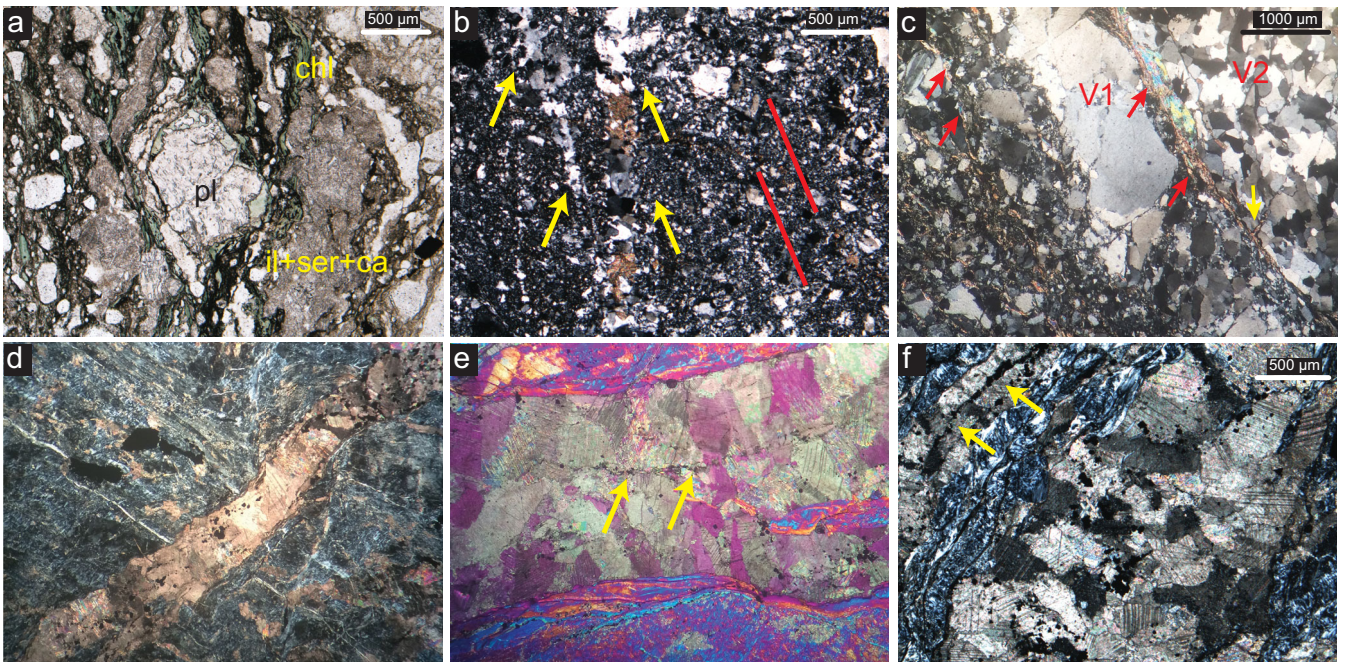

Figure 4. Physical evidence for imprint of fluids in fault rocks from Err Detachment. (a) Saussuritization affects mainly the plagioclase (pl) and produces a chlorite (chl) and illite-sericite-calcite (il+ser+ca) rich-matrix that developed along the cataclastic foliation. The syntectonic clay minerals (phyllosilicates) enriched in Ni-Cr-V. (b) Evidence for fluid flow in the fault. Quartz and calcite veins (yellow arrows) with the same orientation of the cataclastic foliation (red lines). (c) V1 and V2 are different types of blocky quartz veins. The red arrows point to phyllosilicates developed in the matrix of the cataclastic foliation cutting the quartz veins, sometimes with different orientation (yellow arrow). From Figures 4D–4f Calcite veins cutting the serpentinite foliation. Remarkable presence of Fe-oxides in the veins, showing that Fe-rich fluids flowed through fractures. Figures 4e and 4f calcite veins with Fe-oxides in the sealing line (yellow arrows).

of albite, sericite, zoisite, calcite, epidote, chlorite, and quartz veins. The degree of saussuritization increases with deformation. The cataclasites preserve a similar mineralogy to that of the granites. Nevertheless, K-feldspars are altered to albite and to sericite. Plagioclases are also altered and quartz and calcite veins, and dispersed epidote grains are common. The quartz/calcite veins are generally parallel to the cataclastic foliation (Figure 4b), which is defined by the newly formed clay minerals.

Saussuritization leads to the formation of illite, chlorite, calcite, albite, and quartz forming the matrix of foliated cataclasites and gouges (Figure 4a), and a chlorite-muscovite-rich matrix in the clast-rich chlorite-schist. Usually Fe-rich chlorites (chamosite) are found in the rims of plagioclases (Figure 4a). Iron oxides are widely found in the cataclastic foliation. Quartz veins in the fault rocks have blocky textures and, rarely, directional growth textures [*Bons et al.*, 2012]. Most of the veins were deformed by subsequent deformation, in many cases overprinted by the cataclastic foliation (Figure 4c). Toward the core zone, the cataclastic material forms millimetric bands preserving the original fabric at the borders, deformation progressively affect the whole rock which may finally form ultracataclasite and gouges.

The quartz in the fault rocks show patchy extinction and in some samples undulose extinction. Quartz grains also locally underwent bulging process forming subgrains. Gouge and chlorite-schists have an S-C foliation and/or abundant sigma clasts, which were used as kinematic indicators showing a top-to-W and top-to-NW transport direction along the Err detachment system [see also *Froitzheim and Eberli*, 1990; *Manatschal*, 1995]. Similar structures are also found in the Bernina, Chaberton, and Grosina detachment systems. The microstructural characteristics of the studied detachment faults show that they formed at temperature lower than about 300°C and less than 10km depth [*Stipp et al.*, 2002].

3. Methods

3.1. Chemical and Mineralogical Analyses

Bulk-rock chemical and mineralogical analyses were performed on mantle, crustal basement, sedimentary, and fault rocks. Chemical and mineralogical analyses were also made on clay fraction (<2 μm) from fault rocks. The clay fraction was extracted from a sieved <125 μm powder mixed with distilled water (~30 g/

~50 mL H_2O) via repeated centrifuge applications. Mineralogical compositions were obtained from X-ray diffraction analyses (XRD) of nonoriented powders of bulk rocks and from four types of oriented aggregates of the clay fractions (air-dried, ethylene glycol-treated, hydrazine-treated and after heating 4 h at 490°C). The parameters of the D5000 RX Bruker® diffractometer, with a Brucker®DIFFRAC^{plus}-EVA determination program, are: θ–2θ mode, CuKα radiation, 40 kV/30 mA, scan speed 0.02 s^{-1} from 3° to 15° or 3° to 30° (LHyGeS, CNRS-University of Strasbourg).

Chemical analyses are obtained on the samples which were digested using Li–tetraborate fusion followed by dissolution in HNO3-glycerol and all concentration determinations of one sample were carried out from the same fusion. The same method was applied in the three laboratories we used. The samples dried at 100°C, reweighed were ignited at 1000°C for Lost on Ignition (%LOI). Approximately 100 mg of the sample was mixed with 750 mg of lithium tetraborate and melted at ~1000°C. The melt is dissolved in HNO_3-glycerol solution and analyzed by mass spectrometry. At LHyGeS (CNRS-University of Strasbourg), the concentrations were measured with a Thermo Scientific® ICAP 6500ICP-AES and a Thermo Scientific® X Series 2 ICP-MS equipped with collision/reaction cell technology. At SARM-Laboratory (CNRS-Nancy), data are from an ICP-MS Agilent 7700X and ICP-OES Thermo Fischer® ICap 6500. Precision and accuracy of the method were routinely controlled by replicate analyses of the international rock standards [*Govindaraju*, 1995] at both LHyGeS and SARM laboratories. Similar procedures are run by Acme Laboratory (Vancouver, Canada). Total carbon and sulfur were analyzed using Leco equipment (Acme). The achieving precisions for major elements are <2% for concentrations >2%, <5% for the concentrations between 2 and 0.1%, and 10% for the lowest concentrations <0.1%. The precisions for trace elements are <2% for concentrations >100 ppm, <5% for concentrations between 100 and 10 ppm, and <10% for the low concentrations <10 ppm. According to the trace element, the detection limits range from 1 to 0.1 ppm. The elements concentrations given and used in the study are higher above the given detection limits. Some of the serpentinized peridotite data are from *Müntener et al*. [2010] and part of the ED fault rocks data are from *Manatschal et al*. [2000].

3.2. Gain and Losses of Elements

The gain (enrichment) and loss (depletion) of elements during mantle serpentinization and fault rock formation was performed using the modified *Gresens* [1967] approach proposed by *Potdevin and Marquer* [1987], here referred to as *P-M diagrams*. Equation (1) allowed the estimation of concentration variation (ΔC) where c_a and c_o are the concentrations (referred to as mass by some workers, valid for some reference volume) of the altered and the original rock (protolith), ρ_a and ρ_o are the specific gravity of the altered and the original rock, and f treats changes in volume. However, the f-factor is not only related to volume changes during a reaction but implicitly may also account for mass or density variation, as discussed in *Grant* [1986]. Thus, f can be estimated for any given element relative to an immobile element [*Gresens*, 1967; *Grant*, 1986; *Potdevin and Marquer*, 1987; *Manatschal et al*., 2000] assuming some elements are immobile (i.e., $\Delta C=0$). *MacLean and Barrett* [1993] showed that elements such as Al, Ti, and Zr can be used as immobile for many geological processes including hydrothermal alteration. These elements show a good linear correlation between selected protolith and altered rocks (Figure 5), and when plotted on the P-M diagram establish an immobile range (in green on Figures 6, 8, and 9). Therefore, for each of those immobile elements, we have no concentration variation ($\Delta C=0$) and a f value. For graphical purposes, it is assumed a reference value of $\Delta C=-1$ for all elements. Any protolith-altered rock pair of elements can be plotted for their slope $\left(\frac{C_a}{C_o}\cdot\frac{\rho_a}{\rho_o}\right)$ and found to be either enriched or depleted relative to the immobile elements.

This approach avoids problems with linear regression posed by the *Grant* [1986] method, and also is relatively insensitive to problems surrounding the closure rule [*Ague and Van Haren*, 1996]. This is because for any $\Delta C=0$ (immobile element), f is sensitive to both changes in concentration and density. The example of serpentinization (Figure 6b), explored more fully in the following section, is illuminating in this respect because treating Al_2O_3 as immobile results in a $f=1$ whereas an immobile TiO_2 results in an $f \sim 0.75$. Experiments and microstructural evidence show that the serpentinization leads to a volume increase and density decrease [*Evans et al*., 2013; *Kelemen and Hirth*, 2012], but the P-M diagram shows a loss of most mobile elements what is also supported by laboratory experiments on olivine and pyroxene [*Gresen*, 1967; *Ogasawara et al*., 2013]. The magnitude of the volume or density change is thus reflected in the different f-values for the immobile elements. Again, we use immobile elements based on the simple linear

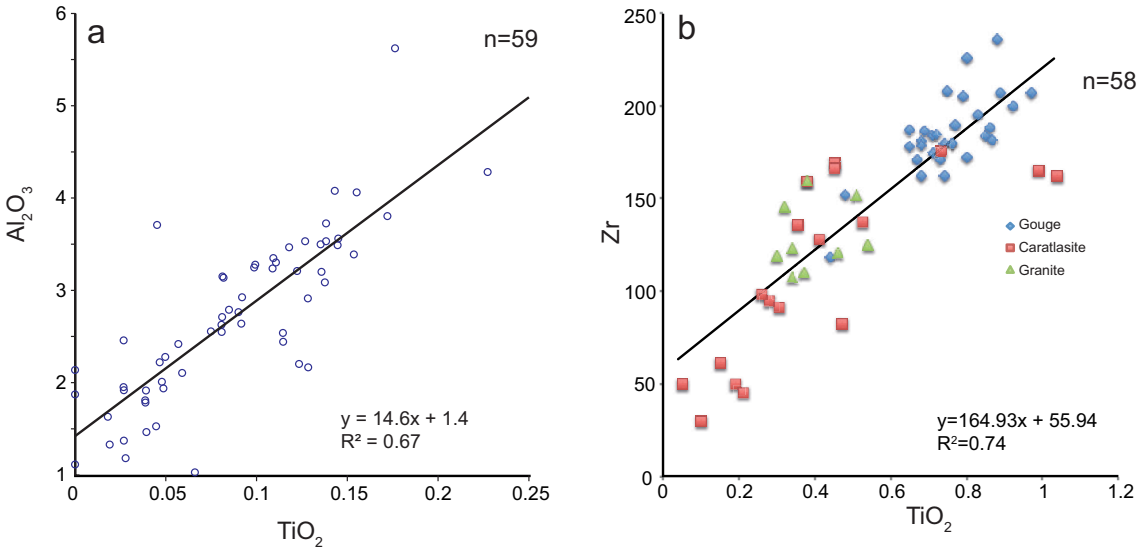

Figure 5. Immobile behavior of elements. Relationship between Al_2O_3, TiO_2, and Zr of the samples from Platta, Malenco, and Err nappes in the Swiss Alps. The linear relationship between these elements evidences their immobile behavior. (a) Al_2O_3 versus TiO_2 in the serpentinized peridotites ranging from 5 to 95% of serpentinization. The good linear correlation is only displaced due three samples that are positioned at the extremities. Data from *Müntener et al*. [2010]. (b) Zr versus TiO_2 from the Albula granite and fault rocks from the Err detachment. Own data from Table 2 and from *Manatschal et al*., [2000].

comparison on Figure 5, and define a band (green on Figures 6, 8, and 9) of immobility with which to compare other elements.

$$\Delta C = \frac{C_a}{C_o} \cdot \frac{\rho_a}{\rho_o} f - 1 \quad (1)$$

This method was applied in the analyses of gains and losses of elements caused by alteration of mantle and continental basement rocks during exhumation. A more descriptive detailed and assumption for each case will be further explained in their respective section.

4. Element Losses During Serpentinization

Using our data (Table 1) and a set of data from *Müntener et al*. [2010], we were able to track the gains and losses of major and trace elements during different stages of serpentinization using the P-M diagram. Petrographical criteria based on thin section analysis and the Loss on Ignition (L.O.I) allowed the characterization of the degree of serpentinization of peridotite from the Upper Penninic nappes (Malenco, Platta and Arosa units), which are in the range of 5–90% (Figure 6a). The samples were grouped in three categories of serpentinization (1) $\leq$10%, (2) 10–60%, and (3) $>$60%. The results of gains and losses are presented for the group 1 to 2 (Figure 6B), from group 2 to 3 (Figure 6C), and from group 1 to 3 (Figure 6D).

Ni, Cr, and V are some of the main trace elements that mark element losses at incipient (Figure 6b) and advanced (Figure 6c) stages of serpentinization. As shown in Figure 7a, samples with low degrees of serpentinization have elevated values while the samples with high degree of serpentinization have low values of Ni-Cr-V, indicating the depletion of these elements. Electron microprobe analyses by *Müntener et al*. [2010] show the mineral controls on the losses of these elements (e.g., Ni and Cr) during serpentinization (Figure 7b).

Apart from Ni-Cr-V, major elements such as Fe, Mn, Mg, Si, and Ca also show important losses, especially at advanced stages of serpentinization (Figure 6c). These observations are supported by the presence of Fe-oxides in late calcite veins (Figures 4d–4f) in ophicalcites and by the occurrence of Fe-oxides spots of about few thousands of square meters and few meters thick in the serpentinites from the Platta nappe. In the Platta nappe, quartz veins are rare and we assume that most of the Si-rich fluids escaped through faults into the overlying seawater and sediments as evidenced by hydrothermal cherts overlying the exhumed mantle.

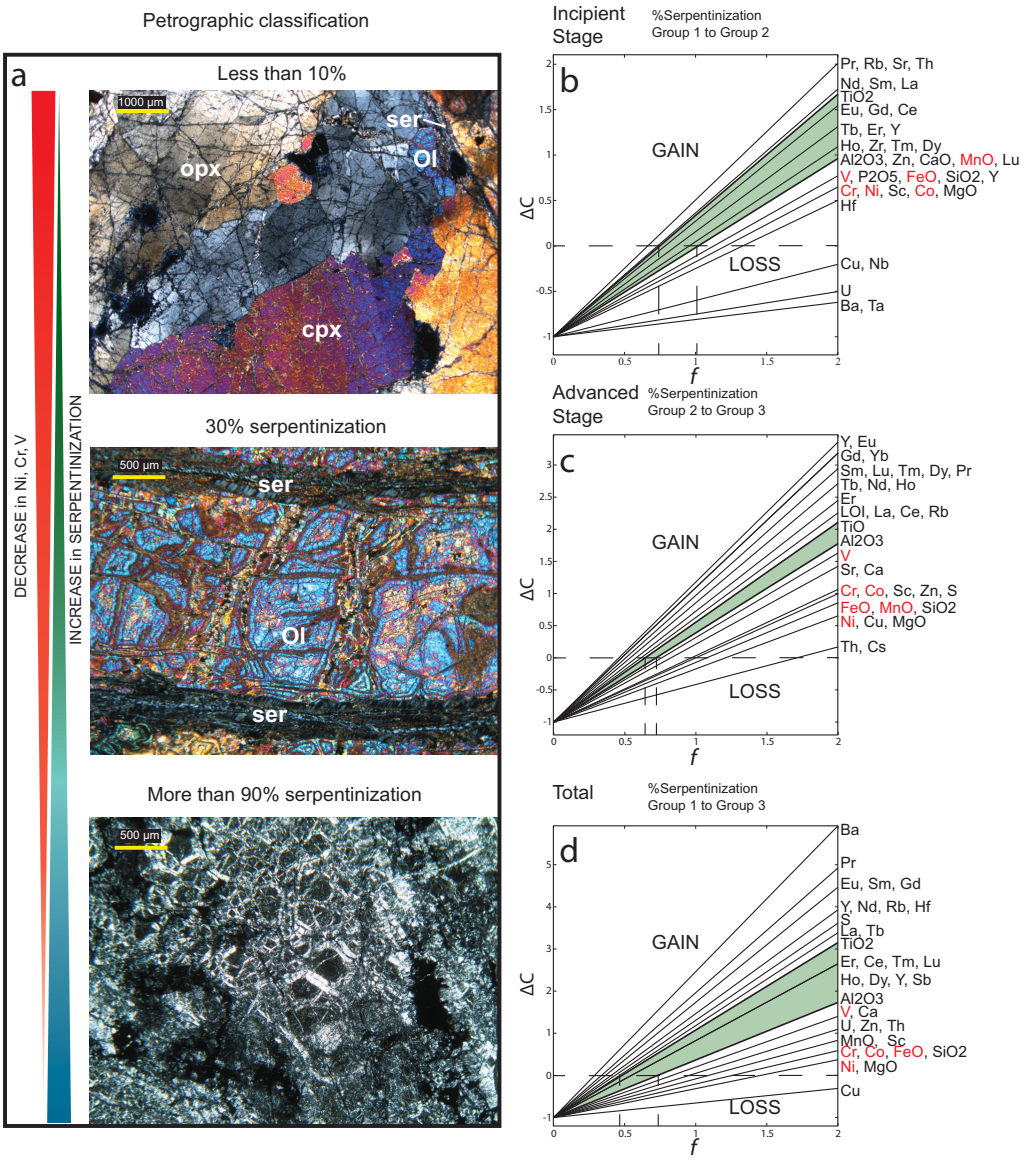

Figure 6. Mineralogical and chemical changes related to serpentinization. (a) The degree of serpentinization (i.e., percentage) is based on petrological criteria and was mainly established by the (olivine+pyroxene)/serpentine ratio. Note that the increase of the degree of serpentinization is accompanied by the decrease of (olivine+pyroxene)/serpentine ratio. According with this ratio, the samples was grouped in three categories. Group 1: samples $\leq$10% serpentinized. Group 2: samples between the interval10–60%. Group 3: samples $>$60% serpentinized. From Figures 6b–6d are the P-M diagrams. Data from Table 1 (this work), and Table 10 and 11 from *Müntener et al.* [2010]. Note the losses in Ni-Cr-V and other elements related to serpentinization. (b) Mass balance at incipient stage defined by weak (Group 1) to moderate (Group 2) degree of serpentinization. (c) Advanced stage defined by moderate (Group 2) to strong (Group 3) degree of serpentinization. Notice in Figure 6d the total losses of elements from weak (Group 1) to strong (Group 3) degree of serpentinization. The specific gravity used for calculation (see equation (1)) are from *Miller and Christensen* [1997]; assumed to be 3.1 g/cc, 2.8 g/cc, and 2.6 g/cc for Group 1, Group 2, and Group 3, respectively.

5. Fluid Signature in Fault Rocks From Extensional Detachment Faults

5.1. Gains and Losses in Fault Rocks From the Err Detachment (ED)

A systematic and elevated gain of elements such Ni, Cr, V, Co, and Cu (Figures 8a–8c and 9) is observed in the fault rocks from the ED. It implies that from protolith to cataclasite to gouge the concentration of these elements increases. Detailed analyses of the ED fault rocks allowed the mapping of the variation of these elements along the footwall of the detachment relative to its distance from the former breakaway. Because the concentration of these elements is higher in clay-rich fault rocks (gouges), the gain of Ni-Cr-V is plotted

Table 1. Peridotite and Serpentinites[a]

Sample Lithology Unit Place Serpent. Degree	Lan-1 Peridotite Lanzo Lanzo *2%*	F3-01 Serpentinite Platta Falotta *95%*	F3-02 Serpentinite Platta Falotta *90%*	P-7 Serpentinite Platta Parsettens *95%*
[b]SiO_2	38.81	32.70	39.58	52.00
[b]Al_2O_3	0.96	20.41	2.08	17.20
[b]Fe_2O_3	10.72	12.67	8.00	12.00
[b]MnO	0.15	0.25	0.12	0.15
[b]MgO	46.38	13.85	36.57	6.83
[b]CaO	0.10	9.39	0.21	1.07
[b]Na_2O	0.02	0.40	<0.01	3.05
[b]K_2O	0.02	<0.01	<0.01	1.89
[b]TiO_2	0.03	1.76	0.06	1.08
[b]P_2O_5	0.02	0.12	<0.01	0.29
LOI	1.50	8.20	12.70	4.26
Sum	98.71	99.75	99.32	99.82
[b]Ba	4.00	7.00	3.00	**90600**
Ce	0.40	17.50	0.40	41.90
[b]Co	140.80	57.20	96.10	22.30
[b]Cr	5747.28	383.15	2415.23	98.80
Cs	<0.1	<0.1	1.10	0.70
[b]Cu	166.30	2.60	10.40	125.20
Dy	0.07	6.26	0.20	4.06
Er	0.04	4.50	0.09	2.35
Eu	<0.02	1.83	0.04	[c]
Gd	0.05	5.39	0.18	4.74
Hf	<0.1	2.70	<0.1	5.94
Ho	<0.02	1.45	0.04	0.89
La	0.30	6.90	0.50	17.89
Lu	0.01	0.68	0.02	0.35
Nb	0.10	3.10	<0.1	15.80
Nd	<0.3	13.60	0.30	19.73
[b]Ni	3107.20	261.10	2230.50	168.00
Pb	0.90	0.40	0.50	28.90
Pr	0.03	2.67	0.04	4.75
Rb	0.90	0.20	0.60	66.50
S	200.00	<0.02	600.00	[c]
Sc	5.00	49.00	8.00	15.28
Sm	<0.05	4.26	0.11	5.37
Sr	0.90	68.30	5.70	4370.00
Ta	<0.1	0.10	<0.1	1.36
Tb	<0.01	0.98	0.03	0.59
Th	<0.2	0.30	<0.2	10.40
Tm	<0.01	0.70	0.02	0.39
U	<0.1	0.20	<0.1	1.48
[b]V	28.00	156.00	46.00	144.60
Y	0.40	35.90	1.20	27.10
Yb	<0.05	4.58	0.10	2.43
[b]Zn	34.00	71.00	20.00	191.10
[b]Zr	1.20	119.10	2.30	227.40
Cd	<0.1	<0.1	<0.1	0.40
Mo	<0.1	<0.1	<0.1	[c]
Sb	<0.1	<0.1	<0.1	0.90
Sn	<1	1.00	<1	4.50
W	<0.5	<0.5	<0.5	1.00

[a]Samples used as end-members. Major elements (oxides) and LOI are in %wt and trace elements are in ppm.
[b]Results from ICP-AES and the other are from ICP-MS, both analyzed in the LHyGeS-CNRS Strasbourg.
[c]Are elements not analyzed. Sample P-7 analyzed at LHyGeS-CNRS Strasbourg and the others at ACME Analytical Laboratories Ltd. Sample P-7 shows exceptional high Ba concentration and correspond to a zone extremely rich in chlorite, quartz veins, and barite.

in Figure 10 in order to outline the variation along the ED as a function of its distance from the breakaway parallel to transport direction.

Ni, Cr, and V were chosen because they are systematically present in all ED fault rocks and, as discussed below, these elements are likely to have originated from the underlying serpentinized mantle. The results in Figure 10 indicate that the more distant the location of the samples is relative to the breakaway of the fault, the higher the concentration of Ni, Cr, and V. In order to test if other faults show the same trend, we also analyzed samples from other detachment faults from the Alpine Tethys.

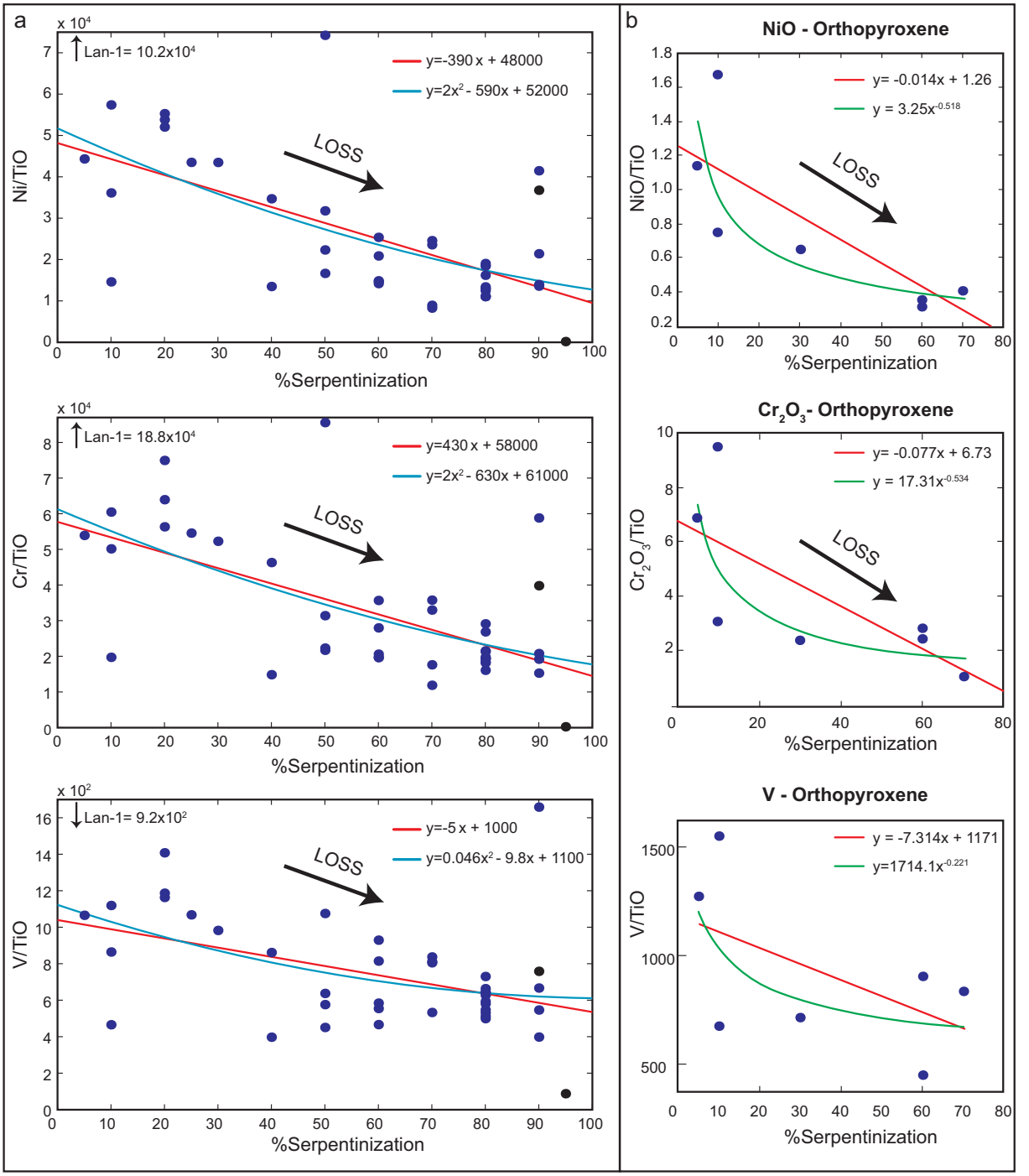

Figure 7. Losses of Ni-Cr-V related to serpentinization. (a) Losses of Ni-Cr-V from bulk rock analyses. Data are from Table 1 (this work), and Table 10 and 11 from *Müntener et al.* [2010]. (b) Losses of NiO, Cr_2O_3, and V in orthopyroxenes as function of serpentinization. The samples are LUM-400, LUM-216, LUM-112, To-7, MSP-1, FAP-6, and SUP-2 from Table 3 and 8 from *Müntener et al.* [2010], which were measured using electron microprobe. Standard deviation (2σ) for TiO_2, NiO, and CrO_2 is usually <0.05.

5.2. Gains and Losses From Detachment Fault Rocks Outside the Err Nappe

In order to evaluate gains and losses from the Chaberton detachment (Figure 8d), we used the average values from the Albula granite exposed under the ED as the protholite and the gouge (CHAB-2) as the altered rock. The choice of ED-footwall Albula granite as a protolith is necessary because only fault rocks are preserved in the Chaberton area. We justify the extrapolation of ED protolith to the Chaberton detachment, because both exhibit similar compositions and mineralogy.

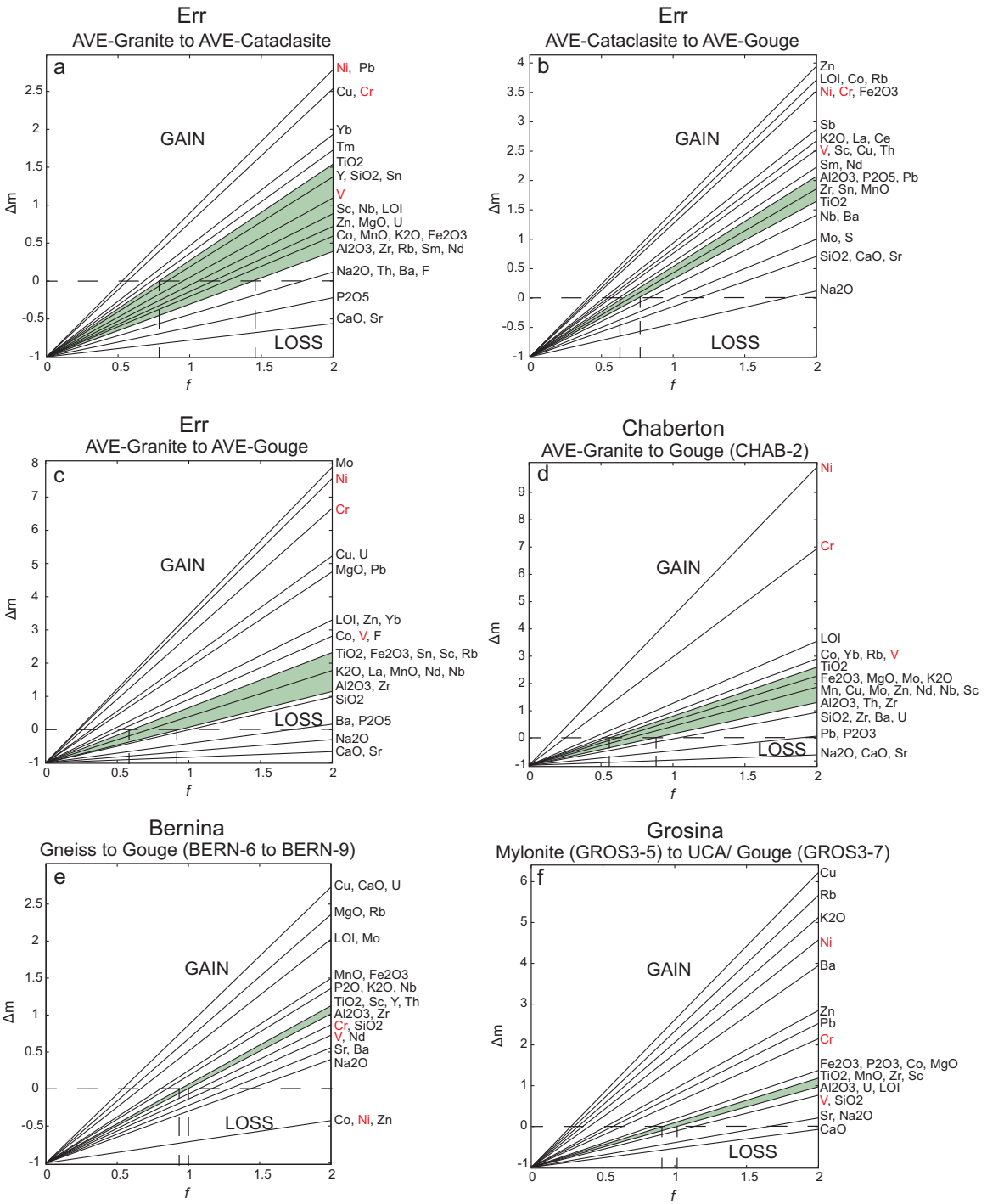

Figure 8. Gain and losses estimated with P-M diagram. From Figures 8a–8c are the result from Err detachment; we used average values from all the Albula granite, cataclasites, and gouges (Table 2) together with averages values from *Manatschal et al.* [2000]. From Figures 8d–8f are the result from Chaberton, Bernina, and Grosina detachments; we used single values from representative samples of these detachments (see text for discussion). The results from Err detachment (c) can be used to compare the differences between other detachment faults (d–f). Observe that gains in Ni-Cr-V from ED are higher than the other detachments. Bernina detachment exhibits losses of Ni-Cr-V and Grosina losses in V. All lines (elements) above the immobile area (in green) are related to element input from outside of the continental crust, which means they are not from the protolith (Albula granite). All lines below the immobile area are losses of elements, meaning they migrated and precipitated elsewhere. Data resulted from ICP-AES/MS analyses (this work) and XRF analyses from *Manatschal et al.* [2000].

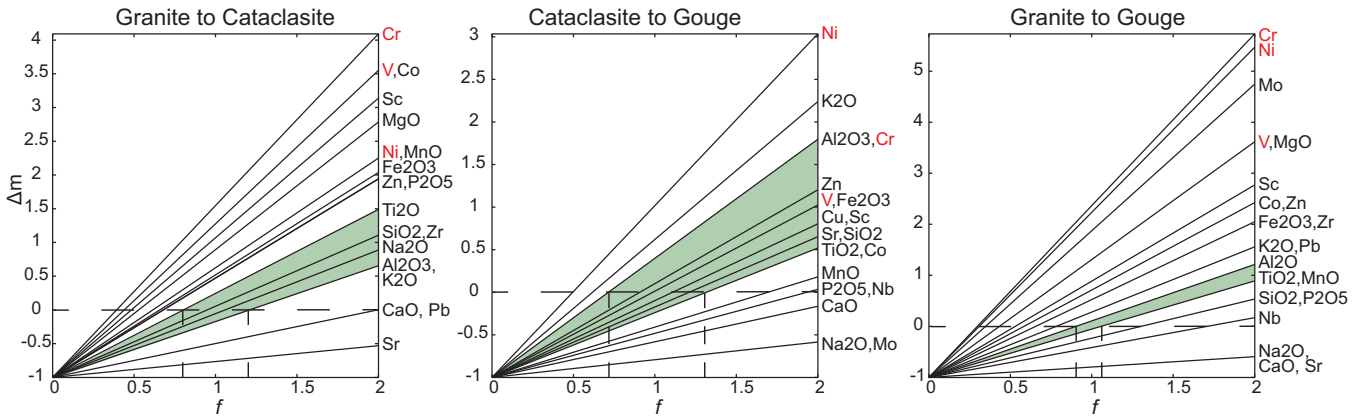

Figure 9. Gain and losses in clay fractions (<2μm) from Err detachment fault rocks. The gain of Ni-Cr-V shows that these elements are likely retained in the neoformed clay minerals instead of the quartz and feldspars of the Albula Granite. The samples used are L-9a for granite, L-7 for cataclasite, and calculated average values of gouges (see Table 3).

In the Bernina detachment (Figure 8e), the transformation from the gneissic protolith (BERN3–6) to a clay-rich ultracataclasite (BERN3–9) shows no gain in Ni-Cr-V. On the contrary, these elements are lost in the fault zone, which is an opposite trend to that observed along the ED.

In the Grosina detachment (Figure 8f), we used the mylonite (GROS3–5) as the protolith and the ultracataclasite (GROS-7) as the altered rock. However, the record of the fluid composition along the Grosina detachment may be more complex by three main reasons: (i) the mineralogical composition, especially the clay content, of the mylonitic protolith changes from place to place, causing different primary quantities of Ni-Cr-V; (ii) the mylonite may have an earlier fluid imprint during mylonitization; and (iii) the interplay between the different detachment systems in the necking zone is not fully understood and a fluid flow interaction between them is possible. Nevertheless, Ni and Cr present minor gain, and V show losses what is opposite to that observed along the ED.

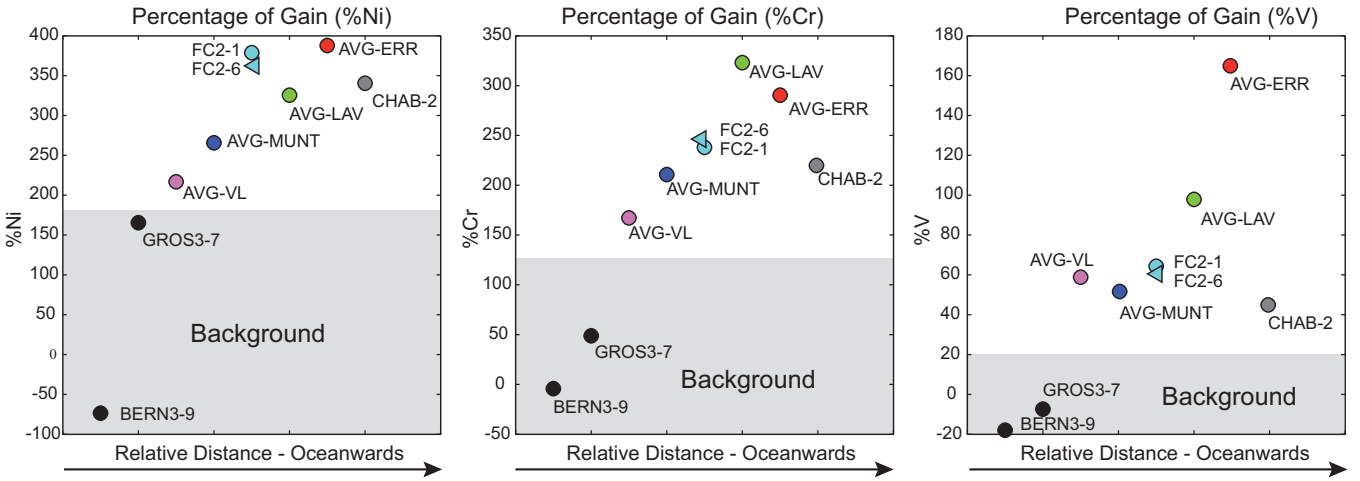

Figure 10. Gain percentage of Ni-Cr-V along detachment faults. To build these figures, we followed three steps. Step-1: we calculated the average values (AVG) of protoliths (e.g., granite) and altered rocks (e.g., gouge) to estimate ΔC, as further explained. The average of the Albula Granite was calculated from our samples in Table 2 and the average from *Manatschal et al.* [2000]. ERR (around Piz Err): samples 1–3 from *Manatschal et al.* [2000]: LAV (around Piz Laviner): our samples from Table 2 with samples 3–5 and 8–12 from *Manatschal et al.* [2000]. VL (Val Lunga): samples in Table 2 with samples 13–19 from *Manatschal et al.* [2000]. FC (Fuorcla Cotschana) and MUNT (Alp Muntatsch) samples from Table 2. For other detachments, we used single samples (see Table 2): GROS (Grosina), BERN (Bernina), and CHAB (Chaberton). The gneiss (BERN3–6) and the mylonite (GROS3–5) were used as protolith for Bernina and Grosina detachment, respectively. For Chaberton, it was used the average value from Albula Granite as protolith. Step-2: assuming no concentration variation ($\Delta C=0$) for Zr, Al, and Ti, we calculated their correspondent *f*-factor. Due to the uncertainties associated with the *f*-factor (see text for explanation), we chose to use an average of *f* calculated as (fZr+fAl+fTi)/3. Step-3: assuming the average of *f*, we calculated using equation (1) the ΔC for Ni, Cr, and V from different segments of the Err detachment as well as the Grosina, Bernina, and Chaberton detachments. The result was multiplied by 100 to have the values in percentage (ordinate-*y*). In the figure, gouges are represented by dots and chlorite-schist by triangles. Note that the sample from Bernina has loss of Ni-Cr-V and from Grosina has little gain of Ni-Cr and loss of V. Grosina detachment was used as background value due to the characteristics of the geological setting. See text for discussion.

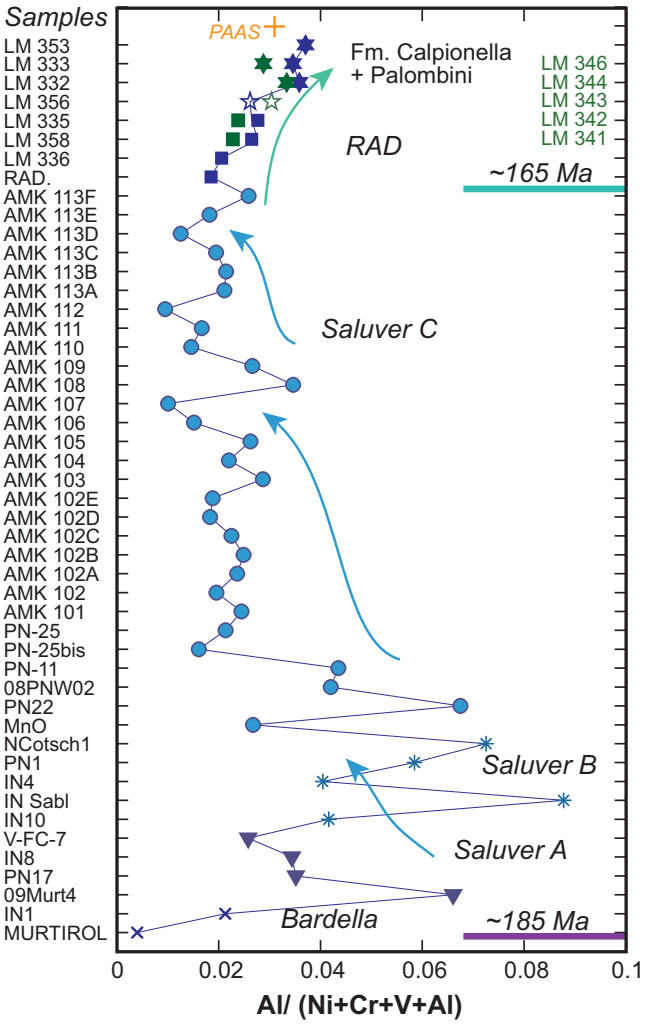

Figure 11. Ni-Cr-V trends from the sedimentary rocks. Samples are located in the ZoS and Murtiröl in the Err nappe (blue symbols). Samples from Platta nappe are from *Bracciali et al.* [2013] (green symbols) and the reference value of PAAS (black cross) from *Condie* [1993]. See caption in Figure 12.

6. The Fluid Signature in the Sediments

Representative sediment sequences where sampled and analyzed (for samples and locations see Table 4 and Figure 2). The main objective was to observe whether the fluids that circulated through the ED also migrated toward the overlain sediments.

Figure 11 exemplifies the increase in Ni-Cr-V concentration from bottom to top of the sedimentary sequence. Although internal variations and spikes can be observed in the Bardella, Saluver A and Saluver B sequences, the average trace metals display a general increase upsection. The Saluver C has a continuous increase in these elements, but the shale-dominated sequence of the Saluver C starts to record a decrease in these elements from the last centimeters (just below the Radiolarite). From this point onward, the regional postrift sequences including Radiolarite, Calpionella, and Palombini formations (it was analyzed the shaly levels) record a continuous decrease in these elements.

Figure 12 shows a continuous increase in Fe and Mn concentrations from the fault rocks to the Saluver C (path1) and a decrease in the regional postrift Radiolarite, Calpionella, and Palombini formations (path 2). These results were compared to other units from the Liguria-Piemont units as well as reference values (NASC and PAAS).

As observed in SEM-BSE images, Fe and Mn are found as braunite (Mn-silicate) and oxides over recrystallized quartz (Figures 13a and 13b), showing the cogenetic relationship between Fe, Mn, and Si. In fact, their concentrations are relatively high in the Saluver C formation, which has variable Fe/Mn ratios and some enrichment in Mn. For reference, we compare the Saluver C composition to similar values as found in Mn and Fe-rich hydrothermally-sourced metalliferous deposits [in *Karpoff et al.*, 1988; *McKenzie et al.*, 1990], as shown in Figure 13c.

7. Discussion

7.1. Tracing Fluids From the Mantle Through the Crust Into Sediments

As indicated on the P-M diagrams, gains of trace elements, such as Ni-Cr-V, in the fault rocks from ED indicate that they should have their source outside the continental crust. These elements were lost during serpentinization leading to their depletion in mantle rocks; other important elements that were mobile include Si, Fe, and Mn. We suggest that serpentinization leads to the enrichment of fluids in the aforementioned elements, and that Ni-Cr-V and Fe-Mn can be used as tracer of a large-scale fluid migration across the

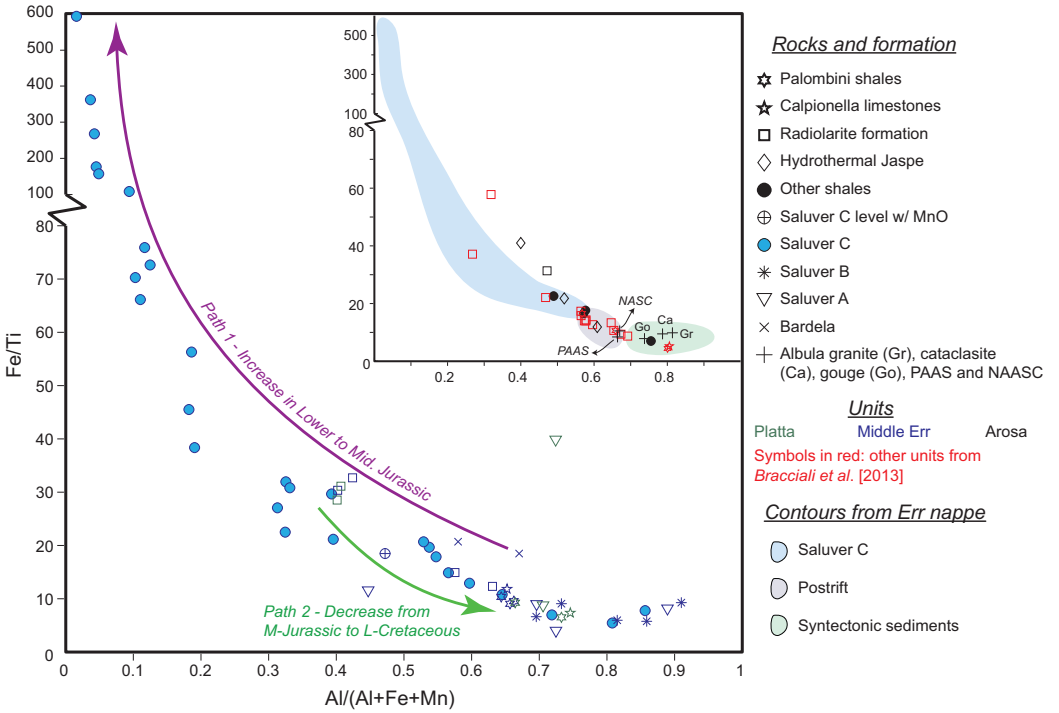

Figure 12. Increase in Fe and Mn from the post tectonic Saluver C sediments. The decrease in Fe and Mn is well marked from the Radiolarite to the Calpionella and Palombini formation (both in Err and Platta nappes). The data of the Radiolarite formation are from this study and *Bracciali et al*. [2013]. Data from Calpionella and Palombini formations are from *Bracciali et al*. [2013]. Reference data are: PAAS (Post-Archean Australian Shale) and NASC (North American Shale Composite) from *Condie* [1993]; Internal Ligurian Units (ILU) and Toscan nappe (TN) in Italy; and Balagne nappe in Corsiga from *Bracciali et al*. [2013] (see Figure 1 for location).

thinned crust, where fluids were channelized along detachment systems. Because these elements are also found in the sedimentary rocks in the supradetachment basin, we suggest that these fluids can also be traced into the overlying sedimentary basins. The fluids likely affected the syntectonic sediments by direct migration and the post tectonic sediments via pollution due to a rising plume of mantle-reacted fluids in the water column. In the following sections, we discuss the different parts of this large-scale hydrothermal system that accompanied the mantle exhumation.

7.1.1. Evidence for Mass Transfer and Fluid Circulation Along Extensional Detachment Faults

Fossil fluid flow in the extensional detachment system can be shown by physical (Figures 3 and 4) and chemical (Figures 8, 9, and 10) evidence. Physical evidence includes: (i) quartz and calcite veins; (ii) iron oxides precipitated in the cataclastic foliation; (iii) syntectonic phyllosilicate minerals transformed or neoformed in the fault zone, which become more abundant toward the core zone of the extensional detachment faults. Chemical evidence includes the products of water-assisted saussuritization process in the extended crust. These processes are responsible for losses of Ca and Si (Figures 8b—8f) and enrichment of fluids in these elements that migrate through the fault zone and precipitate as quartz and calcite veins along the detachment faults (Figures 3a, 3c—3f, and 4b and 4c). Iron oxides found in the foliated cataclasites may be the by-product of alteration of biotite (Figure 8); however, the common occurrence of Fe-oxides and the strong gain of Fe in the gouges and in the cataclasites observed in distal segments of the ED points to an external source for iron. The same is true for a strong redox control on Fe and Mn-oxide alteration [e.g., *Hayman*, 2006]. In addition, large-scale fluid circulation can be demonstrated by the gain of Ni-Cr-V, in which the comparison between the bulk rock (Figure 8) and the clay fraction (Figure 9) analyses, allows us to conclude that trace elements are mainly hosted in syntectonic phyllosilicates (Figures 4a and 4c) from the fault rocks of the ED. As these elements came from outside the surrounding continental basement, they had to be carried by fluids through the active fault zone simultaneously to the formation of the syntectonic phyllosilicate minerals (Figure 14a).

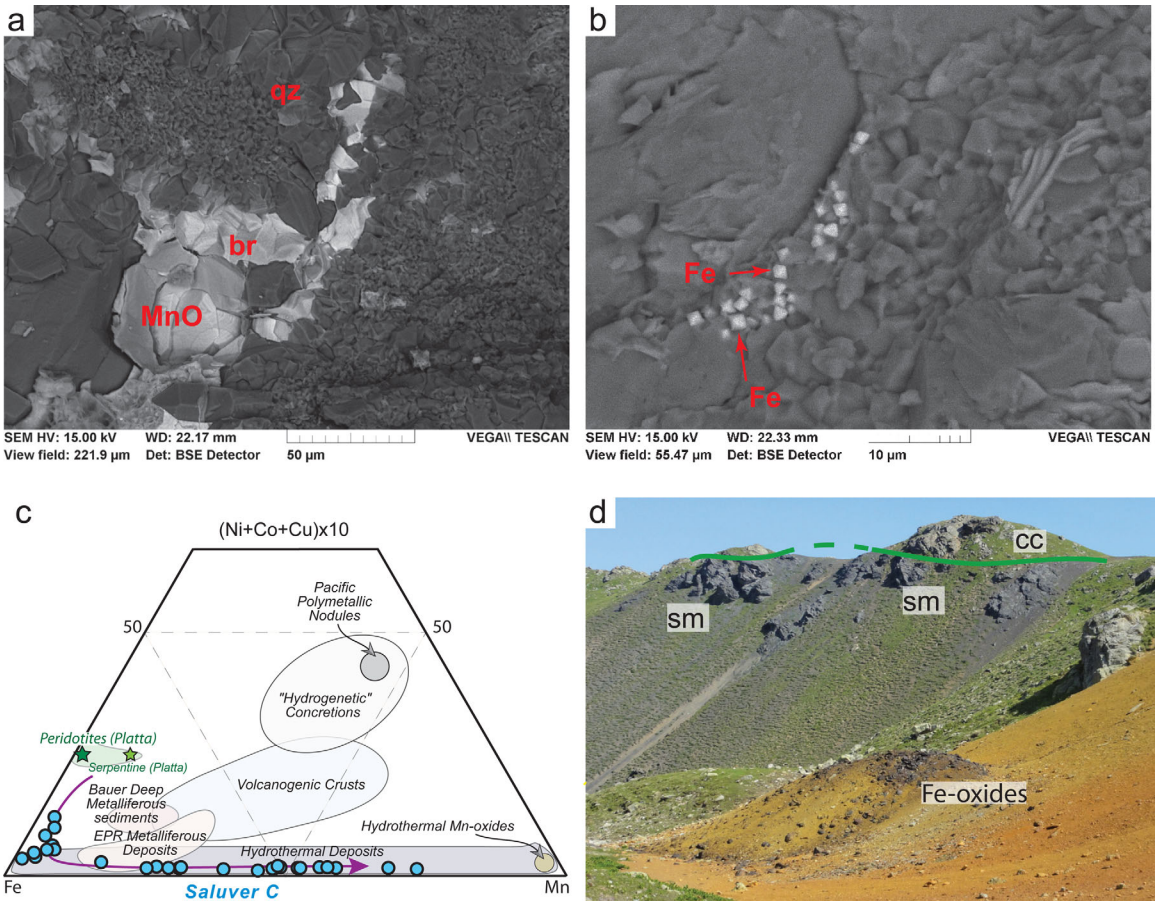

Figure 13. Evidence for Fe and Mn. (a) and (b) SEM-BSE images from Saluver C at ZoS. (a) Braunite (br), Mn-oxide (MnO), and quartz (qz), highlighting the cogenetic relationship between Mn and Si. (b) Iron oxides (Fe) marked by red arrows. (c) Comparison of geochemical data from Saluver C with Fe and Mn from oceanic deposits. Fields in Bonatti diagram from *Karpoff et al*. [1988] and *McKenzie et al*. [1990]. (d) Continental allochthonous block in the ZECM (Parsettens at Platta). The surrounding mantle contains Fe-oxides and high concentration of Barium (sample P7 in Table 1). Continental crust (cc); serpentinized mantle (sm).

7.1.2. Ni-Cr-V: Tracers for Mantle-Reacted Fluids Produced by Serpentinization

The seawater-mantle interaction leads to major serpentinization of olivine and pyroxene and an enrichment of the involved seawater. Once the mantle is not 100% peridotite, and the products of other secondary reactions such as chloritization are observed, we choose the term *mantle-reacted fluids* to designate fluids that show a chemical relation with the mantle rocks. As shown in this study, Ni-Cr-V resulted from losses associated to serpentinization. Their use as tracers for mantle-reacted fluids is justified by: (i) the much higher concentrations in mantle than continental rocks, (ii) the high gains in fault rocks of detachment faults that exhume crustal and mantle rocks (e.g. ED); and (iii) the observation that their concentration is unusually high in the sediments of the distal margin (CDZ).

The elevated gain of Ni-Cr-V in the continental fault rocks along the ED cannot be explained by dissolution/precipitation processes in the surrounding continental basement. Therefore, such enrichment leads to the question about the origin, and how and when the elements were released and migrated upward into the continental crust. These elements show high concentrations in serpentinized peridotites (2000ppm of Ni, 2500ppm of Cr, and 100ppm of V; total of 4600ppm) and even higher in fresh peridotites (Table 1), while they are low in the continental crust. The Albula granite, which represents the main protolith for the fault rocks of the ED, shows very low concentrations (Ni∼6ppm, Cr∼20ppm, V∼45ppm; total of 71ppm, Table 2). Another key observation is that Ni-Cr-V depletion in the mantle (losses) is a function of increasing serpentinization.

Since the deposition of syn to post tectonic sedimentary sequences (Saluver and Radiolarite formations) are contemporaneous with mantle exhumation and they are enriched in Ni-Cr-V (Figure 11), a direct link can be

made between the losses of these elements due to serpentinization and the migration of mantle-reacted fluids toward the basin in the distal margin.

Although Ni-Cr-V are good proxies due to their presence and behavior in all studied systems (i.e., mantle, continental fault zone, and sedimentary sequences), other trace elements such as Cu, Sc, and Co exhibit similar behavior.

Fe and Mn enrichment, as distinct oxides, are also found in the post tectonic sediments (Saluver C) and in the mantle (Figures 4d—4f and 13d). They also suggest a close relationship between serpentinization, mantle exhumation, and fluid transfer.

7.1.3. Formation and Migration of Mantle-Reacted Fluids

Extensional detachment faults in the distal margins cut through a previously thinned, less than 10km thick continental crust and root in the underlying mantle. This triggers a seawater-mantle interaction resulting in the leaching of elements from the mantle during serpentinization, creating a mantle-reacted fluid that migrates through extensional detachment faults. Our observations suggest that serpentinization initiated below the previously thinned crust. This is evidenced by the gain/enrichment in Ni-Cr-V along the ED (Figure 10) and the overlying syntectonic sediments (see following discussion).

The details of how seawater migrates downward into the mantle are not fully understood. But the observation that the signature of the mantle-reacted fluids is registered along the Err detachment fault shows that the seawater somehow migrated downward. Two possibilities, or a combination of the two can be envisaged: (i) seawater flowed downward through synthetic and antithetic high-angle normal faults that are formed in the hanging wall of the detachment; (ii) seawater flowed downward only along detachment faults.

We interpret that the high-angle normal faults also acted as conduits for seawater downward migration as illustrated in the Figures 14a–14d and 15. The progressive downward migration of seawater and serpentinization were intimately linked to the activity of extensional detachment. The serpentinization caused by seawater is evidenced by isotopic work [*Früh-Green et al*., 1990]. The interaction between seawater and mantle rocks had to occur at relatively shallow depths and low temperatures according to the observations discussed in section 4. Nevertheless, considering the stability field of serpentine minerals [e.g., *Moody*, 1976], the temperature, and depth of the fluid-rock interaction and related serpentinization (hydration and chemical exchange) probably were not higher than 420°C. The depth is difficult to estimate, but assuming a thermal gradient of 30°C/km, what may be low for an extending lithosphere, would give 14 km. From refraction seismic data in present-day rifted margins, the thickness of a serpentinization front is up to 6 km [*Dean and Minshull*, 2000]. As the serpentinite layer is exposed to the seafloor at final rifting and the thickness of sedimentary layer is negligible, this would result in a thermal gradient of 70°C/km. Such high thermal gradients may be linked to the thinning of the lithosphere, hydrothermal advection (Figure 14b), and exothermic serpentinization reaction [*Schuiling*, 1964]. Hydrothermal chemical exchange is supported by spots of Fe-oxide crusts (Figure 13d) that are often observed in the serpentinized mantle of the ZECM and by high content of Ba (9%) and barite (see sample P-7 in Table 1, in standard serpentinite Ba=5ppm).

The upwelling of mantle-reacted fluids along the detachment fault record the progressive development of serpentinization that happens when faults were able to cut through the brittle and thinned crust reaching the subcontinental mantle. It is important to emphasize that is unlikely that this upward migration occurred only at a final stage, when the mantle is exhumed to the seafloor. In this context, two major points have to be considered:

1. when a segment of the footwall of the detachment fault is exhumed to the seafloor, it starts to become tectonically inactive and therefore the fluid circulation may decrease due to the healing of fractures (Figure 15) [*Tenthorey and Fitzgerald*, 2006; *Mitchell and Faulkner*, 2012]. In this case, fluids would escape directly to the seawater in the ZECM and it would not be registered all along the ED fault rocks as it was showed in the Figure 10;
2. since fault gouges have low permeability [*Morrow et al*., 1984; *Evans et al*., 1997], fluid migration toward the breakaway throughout the gouge layer seems highly improbable.

However, during fault activity, the permeability can be enhanced [*Tenthorey and Fitzgerald*, 2006]. This is because the fault movement enables fracture opening, especially in the fault zone characterized by cataclastic rocks. The increase of permeability by fracture opening is evidenced by the common occurrence of

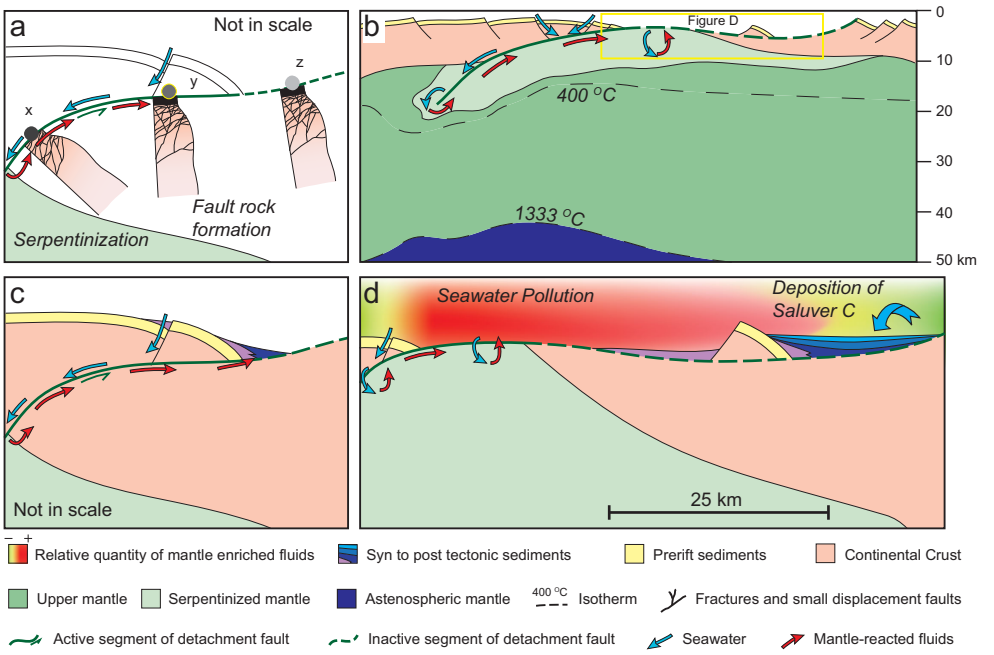

Figure 14. Conceptual processes of fluid migration. (a) Flow of mantle-reacted fluids along the active segment of ED. At the point *x*, the detachment is active and probably with undeveloped gouges. At the point *y*, the detachment is active and gouge are well-developed. At the point *z*, the detachment is inactive. Fluid migration is recorded at the points x and y but not at z. (b) Maximum depth for serpentinization is limited around the 400°C isotherm. The high geothermal gradient may play an important role in the remobilization of elements by controlling convective cells. (c) Direct migration of mantle-reacted fluids toward syntectonic sediments in the supradetachment basin. (d) Seawater Pollution by the rising plume of mantle-reacted fluids spreading in the seawater and interacting with the post tectonic sediments, which is contemporaneous with serpentinization and mantle-exhumation. Note that the segment of detachment fault is active in the ZECM but inactive below the supradetachment basin.

quartz and calcite veins (Si- and Ca-rich fluids) parallel to the brittle foliation in the cataclasites and the observation of polyphase cataclasis suggesting crack sealing mechanisms along the fault.

7.1.4. Fluid Migration Toward the Sedimentary Basin

Direct fluid migration through the ED toward the sedimentary basin is evidenced by Ni-Cr-V enrichments (Figure 11) in the syntectonic sediments (Figures 14c and 16). The flow path in the sedimentary sequences may be very complex due to the porosity-permeability control of the sedimentary rocks. In addition, the sediments, particularly the oldest deposit lying directly on top of the exhumed fault surface, may have been continuously reworked during movements along the underlying detachment fault. Therefore, they may have been affected by small increments of fluid pulses during upward fluid migration. This may explain the spikes of Cr-Ni-V values in the syntectonic Saluver A and Bardella formations (Figure 11). In addition, the rocks were sampled in different places (along strike) in the Zone of Samedan and Murtiröl areas. Within this basal syntectonic sequence, clasts of fault rocks are locally found. But, values of Ni, Cr, and V in these fault rocks are always lower than in the overlying sediments and as the percentage of fault rock clasts in the basal sedimentary sequences is never high, the values measured in these sequences cannot be explained by reworking of fault rocks alone. Thus, a direct contribution of external, mantle-reacted fluids needs to be envisaged to explain the high Cr-Ni-V values in the basal syntectonic sedimentary sequences.

7.1.5. The Pollution of Seawater by the Rising Plume of Mantle-Reacted Fluids: A Record of Mantle Exhumation in Post Tectonic Sediments

The deposition of the Saluver C and Radiolarite formations occurred at the end of activity of Err detachment in the CDZ [*Masini et al*., 2011]. This implies that fluids enriched in Ni-Cr-V and Fe-Mn no longer came from the underlying segment of the ED (Figures 15 and 16). Indeed, the data show that the progressive enrichment persisted even after the end of extension in the distal margin and continued during mantle exhumation in the ZECM. This is supported by elevated Ni-Cr-V values in the Radiolarite formation as well as the occurrence of Ni-Co-Cu and botryoidal Mn-silicates formed under hydrothermal activity in the ZECM [*Perseil and Latouche*, 1989].

AGU Geochemistry, Geophysics, Geosystems

10.1002/2015GC005830

Table 2. Bulk Composition of Fault Rocks[a]

Sample	L-9a Granite	L-9b Granite	BI3-1	AVE-M		MUNTA-1	L-07	FC2–05	FC2–5a	L-7a
Lithology	Middle Err	Middle Err	Granite	Granite	Total	Cataclasites	Cataclasites	Cataclasites	Cataclasites	Cataclasites
Unit Place	Laviner	Laviner	Middle Err	Middle Err	AVE Granite	Middle Err Alp	Middle Err	Middle Err Fuorcla	Middle Err Fuorcla	Middle Err
Lab	SARM	LHyGeS	Val Bever ACME	Zurich	Middle Err	Muntatsch SARM	Laviner SARM	Cotschana SARM	Cotschana SARM	Laviner SARM
SiO_2	67.45	67.60	56.87	68.76	65.17	69.49	73.34	78.87	79.16	74.25
Al_2O_3	15.84	15.80	20.59	14.85	16.77	13.60	12.37	12.82	12.21	12.13
Fe_2O_3	2.70	3.14	4.89	3.52	3.56	3.67	2.48	1.83	1.72	2.18
MnO	0.04	0.05	0.06	0.05	0.05	0.07	0.04	0.02	0.01	0.04
MgO	1.05	1.04	1.41	1.05	1.14	1.94	1.27	0.27	0.26	1.17
CaO	1.53	1.64	6.13	1.75	2.76	0.33	0.62	<0.03	<0.03	0.59
K_2O	3.88	3.82	2.35	3.22	3.32	2.91	3.12	3.22	3.08	3.32
Na_2O	4.03	3.83	3.96	2.65	3.62	4.23	4.01	0.28	0.27	3.88
TiO_2	0.32	0.38	0.62	0.41	0.43	0.35	0.31	1.04	0.99	0.26
P_2O_5	0.17	0.23	0.18	0.58	0.29	0.11	0.22	0.04	0.04	0.21
LOI	1.78	1.61	2.70	1.44	1.88	1.93	1.40	2.29	2.04	1.26
Sum	98.78	99.13	99.76	98.28	98.99	98.62	99.19	100.68	99.78	99.29
As	2.13		<0.5		2.13	5.11	2.48	6.44	6.25	2.25
Ba	724.80	820.90	602.00	543.00	672.68	451.70	324.50	312.90	306.50	340.00
Be	2.77		2.00		2.38	2.13	1.08	2.30	2.13	1.23
Bi	<0.1		<0.1		<0.1	0.32	<0.1	0.33	0.33	<0.1
Cd	<0.12	0.30	<0.1		0.30	<0.12	<0.12	<0.12	<0.12	<0.12
Ce	77.35	118.00	16.60	20.00	57.99	23.96	19.40	73.43	72.63	18.63
Co	3.95	7.00	6.80	10.00	6.94	4.08	3.82	2.79	2.88	3.73
Cr	15.00	31.70	20.53	10.00	19.31	5.42	15.66	60.27	59.41	17.23
Cs	1.79	1.81	3.80		2.47	2.13	1.10	2.94	2.89	1.25
Cu	<5	24.70	5.60	3.00	11.10	8.45	9.89	17.42	21.80	13.71
Dy	3.08	4.08	3.70		3.62	3.04	3.10	6.15	6.13	3.01
Er	1.34	1.92	2.10		1.79	1.84	1.64	3.83	3.75	1.61
Eu	1.20	1.48	1.65		1.44	0.70	0.55	1.41	1.39	0.58
F				647.00	647.00					
Ga	20.07		24.80	13.00	19.29	17.90	14.43	17.12	16.68	14.42
Gd	4.29	6.38	3.65		4.77	2.66	2.69	6.14	5.89	2.67
Ge	1.43				1.43	0.83	1.01	1.78	1.50	0.97
Hf	3.71	5.01	7.50		5.41	3.84	2.53	4.14	4.28	2.81
Ho	0.51	0.77	0.77		0.69	0.62	0.59	1.28	1.26	0.57
In	<0.07				<0.07	<0.07	<0.07	<0.07	<0.07	<0.07
La	40.00	62.61	7.60	20.00	32.55	11.39	9.16	34.50	34.57	8.86
Lu	0.17	0.23	0.33		0.24	0.32	0.22	0.62	0.60	0.22
Mo	<0.5	<0.3	0.20		0.20	<0.5	<0.5	<0.5	<0.5	<0.5
Nb	11.01	16.03	9.40	6.00	10.61	9.02	8.38	14.93	14.42	7.89
Nd	31.19	47.27	11.90	25.00	28.84	10.80	9.79	32.08	32.44	9.52
Ni	9.78	10.00	3.60	3.00	6.59	<5	5.08	8.72	7.95	5.26
Pb	17.86	30.20	5.20	7.00	15.06	5.83	10.91	16.95	16.94	12.29
Pr	8.61	13.10	2.42		8.04	2.88	2.48	8.39	8.46	2.39
Rb	115.70	133.60	141.00	103.00	123.33	94.25	77.94	110.00	107.40	84.20
S				53.00	53.00					
Sb	<0.2	0.50	<0.1		0.50	<0.2	0.20	0.49	0.56	0.21
Sc	7.30	8.46	13.00	11.00	9.94	9.80	8.48	12.49	11.95	7.87
Sm	5.63	8.20	3.26		5.70	2.63	2.62	6.62	6.60	2.59
Sn	1.19	2.70	4.00		2.63	4.19	2.20	2.48	2.65	2.18
Sr	204.50	207.30	340.50	168.00	230.08	70.41	45.50	47.71	47.40	47.20
Ta	1.27	1.87	1.00		1.38	1.16	1.14	1.47	1.41	1.06
Tb	0.59	0.77	0.64		0.67	0.48	0.49	1.01	0.99	0.49
Th	14.19	19.80	3.10		12.36	8.38	4.95	11.15	11.26	4.62
Tm	0.18	0.26	0.34		0.26	0.29	0.25	0.60	0.58	0.24
U	2.04	2.64	4.40		3.03	3.51	3.92	2.62	2.56	2.70
V	28.25	37.50	59.00	70.00	48.69	40.31	37.84	62.79	61.90	34.54
W	0.70	<0.8	0.90		0.80	1.98	0.90	2.05	1.66	0.73
Y	15.36	20.60	19.60	18.00	18.39	18.18	16.75	38.10	37.25	16.42
Yb	1.15	1.57	2.07		1.60	2.03	1.58	4.08	4.04	1.57
Zn	44.32	47.90	61.00	46.00	49.81	62.84	45.89	31.78	32.51	44.42
Zr	145.80	159.70	347.20	123.00	193.93	135.40	91.01	162.00	165.30	98.19

AGU Geochemistry, Geophysics, Geosystems

10.1002/2015GC005830

Table 2. (continued)

L-14 Cataclasites Middle Err Laviner LHyGeS	FC-8C Cataclasites Middle Err Fuorcla Cotschana LHyGeS	FC-8M Cataclasites Middle Err Fuorcla Cotschana LHyGeS	AVE-M Cataclasites Middle Err Zurich	Total AVE Cataclasites Middle Err	FC2–6 Clast-Rich chl-sch Middle Err Fuorcla Cotschana SARM	MUNTA-2 Gouges Middle Err Alp Muntatsch SARM	MUNTA-3 Gouges Middle Err Alp Muntatsch SARM	L-18 Gouges Middle Err Laviner SARM	VL-06 Gouges Middle Err Val Lunga SARM
73.10	85.50	81.00	75.12	76.65	59.88	66.46	62.99	62.55	69.65
11.40	7.16	10.90	11.50	11.57	19.34	14.57	16.79	17.61	12.95
3.75	2.48	2.91	2.24	2.58	8.40	4.23	5.29	6.25	4.99
0.08	0.03	0.03	0.03	0.04	0.11	0.05	0.04	0.07	0.06
1.75	0.34	0.31	0.92	0.92	2.11	2.93	3.43	3.33	2.58
1.28	0.06	0.10	1.32	0.61	0.16	0.34	0.91	0.37	0.50
2.30	1.44	2.34	1.69	2.60	3.64	5.13	4.96	4.73	1.76
2.84	0.65	0.69	3.68	2.28	0.42	1.49	0.77	0.79	3.24
0.53	0.47	0.73	0.27	0.55	0.92	0.48	0.68	0.80	0.44
0.18	0.06	0.06	0.11	0.11	0.16	0.16	0.17	0.17	0.16
2.12	1.30	1.86	1.54	1.75	4.15	3.75	4.91	4.17	3.19
99.32	99.49	100.93	98.42	99.66	99.29	99.57	100.94	100.85	99.52
				4.51	8.35	18.16	72.57	98.78	2.54
731.70	621.50	284.00	361.00	414.87	472.40	467.60	464.10	493.20	128.20
				1.77	2.93	3.33	3.83	5.00	1.85
				0.33	0.34	0.55	0.58	0.70	0.13
0.50	<0.1	0.40		0.45	<0.12	0.49	0.28	0.22	<12
23.52	54.71	79.50	32.00	44.20	92.33	49.16	71.22	87.70	48.78
10.10	6.50	9.10	7.00	5.56	18.24	8.49	10.93	11.55	12.72
36.40	44.40	59.40	8.00	34.02	88.32	47.36	73.10	77.48	15.35
2.19	1.52	2.49		2.06	5.20	12.98	20.10	13.10	2.67
38.80	41.60	22.00	5.00	19.85	26.33	30.54	31.75	32.62	<5
2.38	2.68	4.19		3.84	5.93	4.45	4.88	6.27	2.80
1.29	1.73	2.66		2.29	3.30	2.59	2.74	3.43	1.40
0.59	0.52	0.79		0.81	1.61	0.73	1.04	1.25	0.90
			416.00	416.00					
			8.00	14.76	25.94	18.85	22.18	24.40	14.90
2.39	2.46	4.10		3.63	6.44	4.33	5.27	6.42	3.43
				1.22	2.54	1.46	1.80	2.40	1.47
3.44	2.48	5.29		3.60	5.43	4.22	4.77	6.08	3.18
0.51	0.62	0.97		0.80	1.14	0.89	0.93	1.22	0.51
				<0.07	0.08	0.08	0.10	0.10	<0.07
12.77	28.19	41.46	25.00	22.88	46.36	23.84	36.01	43.58	23.57
0.19	0.26	0.39		0.35	0.49	0.40	0.44	0.50	0.21
<0.3	0.80	1.00		0.90	<0.5	<0.5	0.71	0.70	1.52
7.50	8.39	13.19	4.00	9.75	15.90	9.21	11.72	13.62	7.66
12.54	24.80	35.35	27.00	21.59	38.95	21.98	31.55	38.30	20.65
23.00	23.00	24.00	4.00	12.63	41.45	17.81	30.58	27.05	8.70
28.10	44.70	60.90	59.00	28.40	31.91	41.29	22.82	51.12	6.87
3.20	6.49	9.30		5.45	10.63	5.84	8.46	10.40	5.60
107.20	56.90	94.60	42.00	86.05	142.70	204.30	214.60	198.20	81.92
			454.00	454.00					
0.50	0.60	1.00		0.51	0.90	0.50	1.84	1.20	<0.2
10.52	6.75	10.54	7.00	9.49	18.87	11.61	15.48	17.05	7.68
2.83	4.16	6.39		4.30	7.59	4.63	6.14	7.59	4.27
3.50	2.90	3.80		2.99	3.62	4.67	5.52	5.43	1.89
52.80	40.70	30.30	56.00	48.67	52.39	34.25	39.93	38.94	59.35
0.65	0.75	1.26		1.11	1.49	1.05	1.15	1.26	1.02
0.29	0.35	0.58		0.59	1.00	0.72	0.82	1.03	0.51
4.10	6.40	11.00		7.73	16.71	10.02	13.12	14.93	6.18
0.19	0.28	0.42		0.36	0.49	0.39	0.41	0.50	0.21
2.79	1.20	2.01		2.66	3.40	3.18	4.54	6.04	2.09
76.90	43.40	64.40	44.00	51.79	103.70	59.78	88.35	89.96	53.46
2.10	<0.8	1.20		1.52	1.97	3.47	6.44	3.76	1.45
18.00	16.90	26.00	11.00	22.07	32.64	26.86	27.61	35.08	15.81
1.18	1.75	2.72		2.37	3.22	2.56	2.80	3.35	1.34
46.10	38.40	46.10	42.00	43.34	133.70	111.40	111.40	116.70	54.21
137.40	82.30	175.60	95.00	126.91	207.50	152.10	178.60	226.10	118.40

AGU Geochemistry, Geophysics, Geosystems

10.1002/2015GC005830

Table 2. (continued)

VL-07 Gouges Middle Err Val Lunga SARM	FC2-1 Gouges Middle Err Fuorcla Cotschana SARM	VL-07 Gouges Middle Err Val Lunga SARM	L-16 Gouges/ UCA Middle Err Laviner LHyGeS	AVE-M Gouges Middle Err Zurich	Total AVE Gouges Middle Err	BERN3–6 Gneiss Bernina Val da Fain ACME	BERN3–9 UCA Bernina Val da Fain ACME	GROS3–05 Mylonite Grosina Grosina ACME	GROS3–07 UCA Grosina Grosina ACME	CHAB-2 Gouges Chaberton Chaberton ACME
62.80	61.82	62.59	60.40	62.34	63.51	71.50	67.78	68.75	64.80	62.02
18.13	18.69	18.10	16.40	17.28	16.72	14.57	15.72	14.93	15.70	18.45
4.79	6.52	4.78	6.59	5.75	5.46	2.48	3.07	4.07	5.18	5.72
0.04	0.05	0.03	0.11	0.06	0.06	0.03	0.04	0.07	0.08	0.07
2.90	2.82	2.87	4.05	3.07	3.11	0.93	1.57	1.24	1.51	1.88
0.67	0.21	0.60	0.60	0.56	0.53	0.20	0.37	2.40	1.19	0.52
4.96	5.13	5.02	4.06	4.97	4.52	5.60	6.39	1.90	6.21	5.15
0.90	0.21	0.89	2.33	0.55	1.24	2.29	1.59	4.32	2.79	0.85
0.71	0.87	0.72	0.88	0.77	0.71	0.41	0.45	0.38	0.44	0.78
0.16	0.14	0.16	0.21	0.16	0.17	0.14	0.16	0.08	0.10	0.11
4.51	4.24	3.84	3.44	3.69	3.97	1.70	2.70	1.70	1.80	4.20
100.55	100.68	99.60	99.07	99.20	100.00	99.85	99.84	99.84	99.80	99.75
5.02	26.93	4.94			32.71	26.20	707.00	<0.5	2.00	226.80
519.70	336.40	551.60	674.90	642.00	475.30	657.00	508.00	376.00	992.00	645.00
3.75	3.68	3.78			3.60	5.00	3.00	5.00	<1	<1
0.40	0.44	0.46			0.47	0.30	1.10	<0.1	0.20	0.30
0.13	0.12	0.18	1.90		0.48	0.10	<0.1	<0.1	0.30	<0.1
82.08	92.54	87.48	110.00	75.00	78.22	52.50	45.30	43.40	75.30	90.00
11.42	16.13	12.38	17.70	13.00	12.70	2.70	0.90	7.00	9.00	13.30
64.04	80.71	66.11	149.00	80.00	72.57	20.53	20.53	20.53	34.21	75.26
9.23	8.43	10.03	36.62		14.14	4.00	11.10	2.30	5.90	12.20
24.96	32.87	27.02	73.60	18.00	33.92	18.20	34.90	1.40	5.40	15.10
5.45	5.26	5.82	10.80		5.72	5.91	6.27	4.89	7.20	5.09
3.15	2.89	3.34	7.30		3.36	3.71	3.99	3.36	4.45	2.92
1.20	1.48	1.27	1.24		1.14	0.71	0.70	0.98	1.44	1.31
				1211.00	1211.00					
23.95	24.33	25.15		17.00	21.35	16.20	19.10	16.70	17.60	21.80
5.66	6.11	6.05	9.04		5.79	5.09	5.46	5.27	6.91	6.02
2.55	2.29	2.59			2.08					
4.92	4.86	4.99	6.89		4.99	4.50	4.70	4.10	4.60	5.40
1.09	1.00	1.15	2.60		1.17	1.22	1.38	1.09	1.44	1.06
0.08	0.08	0.09			0.09					
42.05	46.53	44.79	53.80	53.00	40.80	26.00	23.10	25.80	41.80	47.10
0.47	0.45	0.48	0.89		0.48	0.47	0.55	0.53	0.63	0.44
<0.5	<0.5	0.55	0.90		0.87	0.40	0.60	<0.1	<0.1	0.30
12.84	14.36	13.62	12.60	7.00	11.40	7.80	8.90	7.10	8.80	15.20
35.46	39.70	38.59	46.60	27.00	33.31	25.90	21.70	25.50	39.10	40.50
25.15	37.15	26.95	45.00	31.00	27.71	4.80	1.40	7.50	22.30	35.40
26.02	36.00	27.83	147.60	23.00	42.51	26.60	221.00	12.60	23.70	7.90
9.71	10.75	10.37	12.50		9.20	6.70	5.86	6.24	10.51	10.79
192.10	213.30	204.50	228.40	211.00	194.26	186.10	307.40	75.90	270.00	220.40
				415.00	415.00	<0.02	500.00	<0.02	<0.02	1400.00
0.33	1.01	0.42	1.40		0.96	0.30	1.30	0.10	0.20	0.40
15.53	17.14	15.50	19.21	23.00	15.80	8.00	9.00	12.00	14.00	13.00
6.92	7.61	7.40	9.34		6.74	5.50	5.10	4.87	8.19	7.36
4.41	3.74	4.61	4.80		4.38	9.00	30.00	4.00	5.00	4.00
33.77	26.30	36.29	44.00	28.00	37.87	41.10	32.60	252.40	175.90	34.70
1.31	1.33	1.34	1.03		1.19	0.60	1.00	0.90	0.90	1.10
0.91	0.92	0.97	1.66		0.94	0.89	1.00	0.83	1.23	0.91
15.02	16.00	15.39	13.60		13.03	12.00	13.30	10.40	15.70	14.50
0.47	0.43	0.50	1.18		0.51	0.55	0.58	0.54	0.67	0.47
5.38	3.12	5.44	42.51		9.04	3.10	5.60	4.10	4.30	2.70
71.41	97.19	76.43	120.30	139.00	88.43	42.00	36.00	54.00	56.00	86.00
3.49	4.62	3.23	4.90		3.92	11.20	19.20	<0.5	0.70	4.70
32.10	29.04	33.56	70.30	30.00	33.37	32.80	36.50	33.20	37.50	28.60
3.08	2.86	3.28	7.02		3.29	3.48	3.69	3.41	4.32	3.05
88.28	107.90	88.66	137.30	120.00	103.98	81.00	23.00	39.00	80.00	71.00
174.30	181.50	184.70	235.60	185.00	181.81	162.30	160.90	134.10	153.40	187.50

[a]Granite is related to Albula granite, cataclasite also refers to foliated cataclasites. AVE-M means average values from *Manatschal et al.* [2000] (Zurich) and Total AVE refers to the total average from each rock type. Analyses were carried using ICP-MS and ICP-AES (see Table 1) in the LHyGeS-CNRS Strasbourg, Service d'Analyse des Roches et des Minéraux (SARM)-CNRS-CRPG at Nancy and Acme Analytical Laboratories Ltd. Major elements (oxides) and LOI are in %wt and trace elements are in ppm.

Table 3. Composition of Clay Fraction From Err Detachment Fault Rocks[a]

Sample Lithology Unit Place	L-9b Granite Middle Err Laviner	L-07 Cataclasite Middle Err Laviner	L-18 Gouge Middle Err Laviner	MUNTA-2 Gouge Middle Err Alp Muntatsch	MUNTA-3 Gouge Middle Err Alp Muntatsch	VL-06 Gouge Middle Err Val Lunga	VL-07 Gouge Middle Err Val Lunga	FC2-1 Gouge Middle Err Fuorcla Cotschana	AVE-GO Gouge Middle Err -
SiO_2	55.11	58.05	46.39	49.22	46.33	51.11	47.51	46.99	47.93
Al_2O_3	21.68	17.41	24.50	21.21	23.83	21.20	26.38	26.84	23.99
Fe_2O2	4.92	7.47	8.23	7.48	.77	8.71	6.00	7.35	7.59
MnO	0.08	0.13	0.09	0.10	0.06	0.11	0.04	0.06	0.08
MgO	2.14	4.05	4.75	5.34	.20	5.57	4.06	3.70	4.77
CaO	1.89	0.89	0.31	0.39	0.52	0.40	0.43	0.18	0.37
Na_2O	3.38	3.15	0.33	0.74	0.36	1.92	0.36	0.21	0.65
K_2O	5.51	4.34	7.59	6.82	7.05	4.56	8.11	8.03	7.03
TiO_2	0.49	0.61	.40	0.59	0.41	0.55	0.48	0.35	0.46
P_2O_5	0.17	0.25	0.17	0.18	0.09	0.12	0.07	<0.04	0.13
LO.I	4.33	4.28	6.40	6.43	6.91	5.73	6.24	5.99	6.28
Sum	99.70	100.63	99.16	98.50	98.53	99.98	99.68	99.70	99.28
As	9.92	7.51	240.90	29.24	120.50	6.12	6.61	50.03	75.57
Ba	734.40	492.90	848.50	513.20	688.70	385.20	923.00	532.40	648.50
Be	4.61	2.74	8.05	6.06	6.47	3.54	5.70	5.28	5.85
Bi	<0.1	0.11	1.49	1.10	1.07	0.26	0.52	0.54	0.83
Cd	0.28	0.14	0.25	0.88	0.42	<0.12	0.12	0.12	0.36
Ce	56.24	28.40	46.59	65.29	74.75	98.97	125.30	49.36	76.71
Co	13.73	31.24	26.22	28.13	25.46	19.23	16.61	25.44	23.52
Cr	29.68	75.57	128.00	91.33	119.90	33.41	99.41	127.40	99.91
Cs	6.43	3.23	30.08	29.62	45.41	9.95	18.21	15.11	24.73
Cu	8.12	52.90	65.78	58.63	65.99	10.82	39.30	51.33	48.64
Dy	2.66	5.74	6.22	8.04	6.45	4.59	6.11	2.70	5.69
Er	1.14	3.03	3.68	4.53	3.51	2.13	3.03	1.48	3.06
Eu	1.33	1.10	0.92	1.20	1.20	1.69	1.59	0.71	1.22
Ga	36.50	32.90	36.07	34.45	34.75	28.88	37.58	36.67	34.73
Gd	3.44	5.40	6.06	7.19	6.19	6.07	7.26	2.91	5.95
Ge	1.60	1.51	3.23	2.64	2.25	2.51	3.45	2.56	2.77
Hf	0.76	0.90	1.08	1.88	1.15	0.82	0.75	1.87	1.26
Ho	0.45	1.10	1.28	1.59	1.26	0.81	1.11	0.52	1.10
In	<0.07	0.18	0.17	0.15	0.16	0.11	0.13	0.12	0.14
La	28.53	14.30	21.92	31.59	37.95	48.16	65.43	27.18	38.71
Lu	0.14	0.42	0.55	0.64	0.50	0.30	0.39	0.24	0.44
Mo	0.57	9.00	1.46	<0.5	1.56	2.92	0.61	<0.5.	1.64
Nb	16.62	18.80	9.07	11.64	8.04	9.25	12.23	8.09	9.72
Nd	22.91	17.39	22.41	30.55	33.17	39.47	54.67	19.60	33.31
Ni	16.27	26.09	128.00	36.71	52.03	19.78	32.36	46.88	52.63
Pb	46.77	19.35	109.09	80.68	32.74	14.55	36.47	47.70	53.54
Pr	6.21	3.99	5.59	7.97	8.96	10.99	14.91	5.50	8.99
Rb	241.10	135.10	351.10	322.80	343.00	215.00	349.00	367.00	324.65
Sc	12.60	26.07	23.06	23.45	24.71	21.43	23.43	24.93	23.50
Sb	0.42	0.45	2.10	0.76	3.06	0.39	0.48	1.29	1.35
Sm	4.22	4.99	5.61	7.01	6.66	7.98	10.06	3.61	6.82
Sn	2.04	6.44	8.40	9.19	8.81	5.77	6.94	5.58	7.45
Sr	168.50	39.54	38.12	24.78	38.79	34.63	41.40	27.83	34.26
Ta	1.96	2.60	0.76	1.27	0.70	1.25	0.99	0.65	0.94
Tb	0.51	0.94	0.99	1.28	1.06	0.88	1.09	0.47	0.96
Th	25.20	15.43	28.34	18.84	19.32	15.16	23.53	10.89	19.35
Tm	0.16	0.45	0.56	0.68	0.53	0.32	0.43	0.22	0.46
U	2.25	7.52	10.69	5.30	4.98	2.37	6.77	2.31	5.40
V	56.55	130.00	141.90	112.20	146.20	123.10	116.20	143.80	130.57
W	0.96	11.65	2.87	3.98	4.67	1.34	3.55	3.55	3.33
Y	13.17	31.40	36.29	45.78	36.17	24.39	29.11	14.44	31.03
Yb	0.99	2.95	3.66	4.45	3.49	2.03	2.71	1.57	2.99
Zn	95.39	140.40	173.50	215.70	188.80	116.50	112.70	130.10	156.22
Zr	27.34	28.34	38.38	62.29	38.62	24.88	22.62	63.44	41.71

[a]Granite is related to Albula granite. AVE-GO refers to the average of gouges samples. The clay fraction separation (<2 μm) were carried at LHyGeS-CNRS Strasbourg using centrifugation technic. Elemental analyses results from ICP-MS and ICP-AES (see Table 1) at SARM-CNRS-CRPG at Nancy (see Table 1). Major elements (oxides) and LOI are in %wt and trace elements are in ppm.

It is important to mention that the concentrations of Ni-Cr-V and Fe-Mn in the Saluver C are higher than in the shales from the Radiolarite formation that is in direct contact with the serpentinites and seals the exhumed mantle in the ZECM (Figure 16). This may suggest that when the Radiolarite formation was deposited, mantle exhumation was diminishing (or ended) and that the mantle was more

Geochemistry, Geophysics, Geosystems

10.1002/2015GC005830

Table 4. Composition of Bulk Sedimentary Rocks[a]

Name Lithology Unit Sample	Murtirol Bardella Middle Err Murtirol	IN1 Bardella Middle Err Il Nes	09Murt4 Saluver A Middle Err Murtirol	PN17 Saluver A Middle Err Piz Nair	IN8 Saluver A Middle Err Il Nes	VA-FC-7 Saluver A Middle Err Fuorcla Cotschana	IN10 Saluver B Middle Err Il Nes	IN Sabl Saluver B Middle Err Il Nes	IN4 Saluver B Middle Err Il Nes	PN1 Saluver B Middle Err Piz Nair
[b]SiO_2	6.70	15.71	79.44	69.99	83.69	61.80	61.28	58.32	86.80	76.04
[b]Al_2O_3	0.68	2.45	12.38	14.21	7.76	15.30	13.07	8.13	7.26	10.69
[b]Fe_2O_3	0.19	1.30	1.13	4.65	2.13	14.10	3.54	0.58	2.38	1.77
[b]MnO	0.06	0.04	0.03	0.04	0.09	0.19	0.06	0.03	0.02	0.06
[b]MgO	24.40	15.50	0.63	1.95	0.70	0.84	4.14	6.33	0.50	1.69
[b]CaO	29.00	25.30	0.32	0.31	0.21	0.02	4.15	8.16	0.13	2.00
[b]Na_2O	0.55	0.41	3.09	1.36	0.76	0.65	1.40	1.74	0.25	2.12
[b]K_2O	2.21	0.59	2.04	2.93	1.41	1.85	2.40	2.56	1.68	2.36
[b]TiO_2	0.01	0.07	0.16	0.60	0.62	1.42	0.46	0.07	0.42	0.35
[b]P_2O_5	0.62	0.24	0.43	0.37	0.39	0.07	0.36	0.58	0.33	0.36
L.O.I	34.84	38.59	1.45	2.54	1.41	3.06	8.91	13.84	1.31	3.92
Sum	99.26	100.20	101.11	98.95	99.17	96.24	99.76	100.34	101.08	101.34
[b]Sr	111.70	154.50	16.70	39.30	22.40	33.90	50.60	42.00	31.20	64.00
[b]Ba	32.90	30.80	84.80	359.20	277.20	289.90	248.90	87.10	130.60	110.80
[b]V	9.90	21.80	16.60	83.60	38.00	119.90	65.20	9.30	29.00	32.60
[b]Ni	66.20	24.80	59.00	51.60	37.30	100.00	41.90	25.40	36.10	36.50
[b]Co	5.00	1.70	3.30	9.60	4.50	25.00	7.50	1.50	3.40	5.10
[b]Cr	14.00	13.00	17.00	71.00	40.00	85.90	52.00	10.00	26.00	22.00
[b]Zn	70.00	20.00	30.00	80.00	100.00	200.20	70.00	40.00	50.00	50.00
[b]Cu	10.00	20.00	10.00	30.00	10.00	65.90	30.00	20.00	20.00	30.00
[b]Sc	<0.07	<0.07	<0.07	<0.07	<0.07	20.92	<0.07	<0.07	<0.07	<0.07
[b]Zr	4.00	20.00	73.00	149.00	484.00	235.20	113.00	35.00	120.00	119.00
Y	8.60	6.20	16.20	27.80	13.70	47.00	26.60	23.20	12.60	18.20
Th	0.70	1.50	4.50	11.70	11.80	14.60	9.60	5.70	7.40	6.80
U	0.73	2.69	0.78	1.69	2.20	3.68	1.44	1.06	1.34	1.14
Rb	34.20	18.30	111.20	151.40	72.30	60.40	124.00	102.50	103.60	104.50
Cs	2.03	0.54	1.97	2.18	1.52	1.30	2.25	0.98	2.35	2.12
Nb	0.62	1.94	5.54	12.78	10.97	18.11	9.78	3.81	7.29	9.15
Mo	<0.3	<0.3	<0.3	<0.3	<0.3	0.50	<0.3	<0.3	<0.3	<0.3
Sb	<0.3	<0.3	<0.3	<0.3	<0.3	0.90	0.30	<0.3	0.40	<0.3
Hf	0.11	0.55	2.28	4.37	12.49	5.76	3.25	1.52	3.23	3.34
Ta	0.03	0.20	0.96	1.05	0.91	1.93	0.92	1.12	0.77	1.22
W	1.50	0.90	2.90	4.90	1.10	1.40	2.20	1.10	2.10	1.70
As	2.70	<0.9	1.30	1.30	3.80	[c]	7.50	2.80	9.70	1.40
Pb	<0.4	<0.4	0.60	2.40	2.30	67.40	2.60	0.50	1.20	1.00
Cd	0.15	<0.15	<0.15	0.07	0.13	0.40	0.06	<0.15	<0.15	0.06
Sn	1.10	1.00	1.90	2.80	3.50	3.90	2.40	1.80	3.70	2.30
La	5.51	5.10	9.29	33.85	22.41	41.27	25.59	23.06	19.92	8.61
Ce	10.09	11.14	19.48	69.78	45.08	82.45	58.35	26.88	38.39	24.51
Pr	1.17	1.41	2.32	8.20	5.26	9.62	5.98	5.22	4.42	2.63
Nd	4.56	5.54	8.50	30.30	19.24	36.04	22.28	19.33	16.20	10.23
Sm	0.96	1.19	1.99	5.80	3.30	7.86	4.33	3.55	2.71	2.27
Eu	0.21	0.18	0.25	1.01	0.58	1.18	0.77	0.34	0.49	0.35
Gd	0.92	1.05	1.89	5.00	2.59	7.07	3.76	2.93	2.16	2.09
Tb	0.16	0.17	0.40	0.81	0.38	1.11	0.63	0.48	0.36	0.41
Dy	0.86	1.01	2.52	4.88	2.14	6.61	4.08	2.95	1.98	2.60
Ho	0.20	0.21	0.52	1.00	0.46	1.47	0.90	0.66	0.41	0.57
Er	0.48	0.54	1.38	2.72	1.31	3.92	2.50	1.75	1.09	1.59
Tm	0.08	0.09	0.25	0.45	0.24	0.63	0.44	0.30	0.20	0.29
Yb	0.46	0.53	1.53	2.84	1.65	3.77	2.65	1.87	1.23	1.85
Lu	0.07	0.08	0.21	0.41	0.28	0.54	0.39	0.28	0.18	0.28

AGU Geochemistry, Geophysics, Geosystems

10.1002/2015GC005830

Table 4. (continued)

NCotsch1 Saluver B Middle Err Fuorcla Cotschana	MnO Saluver C Middle Err Piz Nair	PN22 Saluver C Middle Err Piz Nair	08PNW02 Saluver C Middle Err Piz Nair	PN-11 Saluver C Middle Err Piz Nair	PN-25bis Saluver C Middle Err Piz Nair	PN-25 Saluver C Middle Err Piz Nair	AMK 101 Saluver C Middle Err Piz Nair	AMK 102 Saluver C Middle Err Piz Nair	AMK 102A Saluver C Middle Err Piz Nair
77.86	58.68	82.92	73.54	78.97	48.92	77.13	67.68	53.83	76.19
10.64	2.60	8.08	8.68	9.12	2.48	7.03	11.00	6.20	11.00
1.30	1.64	1.01	1.51	2.55	17.58	6.95	8.84	16.50	6.23
0.02	0.51	0.01	0.04	0.14	20.07	1.14	3.51	14.80	0.14
1.34	6.93	0.59	2.32	1.75	0.50	1.85	1.61	0.69	1.80
1.03	11.00	0.35	2.77	0.49	0.61	0.82	0.39	0.57	0.18
1.82	0.58	2.25	3.06	1.44	0.53	0.26	1.17	0.75	0.99
3.36	0.51	1.77	1.38	2.66	0.66	1.14	2.48	1.63	2.38
0.26	0.10	0.15	0.33	0.43	0.12	0.27	0.49	0.27	0.49
0.42	0.16	0.32	0.32	<0.05	0.16	0.11	0.16	0.17	0.16
2.92	17.64	1.12	5.32	2.18	7.72	2.45	3.64	5.82	2.29
100.97	100.36	98.57	99.27	97.58	91.63	96.70	100.96	101.23	101.86
16.50	87.10	16.40	74.80	36.90	199.20	60.10	112.40	180.90	32.60
131.50	55.60	114.30	96.50	166.30	39.00	99.70	311.30	145.40	208.60
17.80	22.80	11.80	40.50	53.10	43.40	61.60	104.80	80.60	122.50
34.20	11.30	34.30	40.30	21.00	27.00	66.00	77.30	54.90	60.30
3.00	2.30	2.00	27.10	7.53	62.87	32.44	30.92	61.43	28.03
20.00	16.00	13.00	24.00	32.00	10.00	43.00	50.00	29.00	58.00
40.00	10.00	40.00	40.00	82.00	82.00	115.00	87.00	109.00	96.00
20.00	10.00	20.00	20.00	31.96	40.58	65.74	70.70	72.60	53.70
<0.07	1.00	<0.07	<0.07	7.50	4.50	7.20	11.00	7.00	10.00
83.00	17.00	91.00	105.00	156.00	32.00	64.00	108.00	66.00	99.00
13.20	3.20	26.10	16.90	24.80	33.80	26.20	25.40	29.80	18.80
7.00	<0.3	9.90	6.10	10.60	2.06	4.95	8.83	5.01	8.25
1.08	<0.07	1.57	2.06	2.61	1.01	1.23	1.85	1.52	1.45
122.40	13.90	83.40	60.90	117.72	19.12	43.29	103.50	64.30	96.20
1.57	11.71	1.22	1.06	4.11	0.96	1.86	5.91	2.90	4.05
6.92	1.55	6.58	6.78	9.85	2.34	5.10	12.25	7.47	11.87
<0.3	1.60	<0.3	<0.3	0.60	2.47	0.76	0.97	0.97	0.38
<0.3	5.43	<0.3	<0.3	0.31	0.30	0.33	1.20	0.80	1.40
2.43	<0.03	3.48	3.14	4.76	0.75	1.70	2.86	1.75	2.67
0.87	3.90	0.99	0.80	1.30	0.21	0.47	0.86	0.50	0.80
1.70	1.70	1.50	1.90	8.07	6.37	7.67	2.80	1.80	2.40
1.00	2.80	<0.9	1.30	c	c	c	1.20	12.80	1.20
0.50	1.26	<0.4	2.10	13.02	45.74	56.99	16.10	56.40	19.40
<0.15	0.60	<0.15	<0.15	c	c	c	c	c	c
1.60	<0.4	1.70	9.50	c	c	c	c	c	c
12.07	1.24	10.23	12.56	15.64	14.17	18.77	28.74	20.71	25.04
31.09	4.71	25.77	25.31	37.27	38.41	50.13	69.83	50.14	56.45
3.19	0.87	2.74	3.07	4.00	3.60	4.66	6.14	4.76	5.46
11.76	0.17	9.84	11.60	15.17	15.51	18.62	21.20	19.40	19.70
2.33	0.73	2.11	2.53	3.15	4.06	4.11	3.70	4.64	3.64
0.29	0.10	0.22	0.37	0.50	1.00	0.83	0.91	1.21	0.82
1.94	0.63	2.10	2.26	2.72	3.66	3.35	3.83	4.66	3.43
0.32	0.13	0.44	0.42	0.52	0.60	0.57	0.59	0.68	0.50
1.99	0.40	3.30	2.60	3.49	3.90	3.53	3.83	4.21	3.06
0.43	0.06	0.78	0.56	0.77	0.89	0.74	0.88	0.98	0.67
1.20	0.37	2.32	1.49	2.24	2.47	1.98	2.26	2.62	1.72
0.21	0.05	0.45	0.27	0.38	0.43	0.31	0.38	0.45	0.27
1.31	0.50	2.94	1.65	2.59	2.66	1.80	2.42	2.91	1.75
0.19	0.13	0.46	0.25	0.37	0.38	0.28	0.40	0.49	0.27

Geochemistry, Geophysics, Geosystems

10.1002/2015GC005830

Table 4. (continued)

AMK 102B Saluver C Middle Err Piz Nair	AMK 102C Saluver C Middle Err Piz Nair	AMK 102D Saluver C Middle Err Piz Nair	AMK 102E Saluver C Middle Err Piz Nair	AMK 103 Saluver C Middle Err Piz Nair	AMK 104 Saluver C Middle Err Piz Nair	AMK 105 Saluver C Middle Err Piz Nair	AMK 106 Saluver C Middle Err Piz Nair	AMK 107 Saluver C Middle Err Piz Nair	AMK 108 Saluver C Middle Err Piz Nair
75.57	70.97	58.23	48.30	74.10	81.64	76.11	41.22	65.75	45.27
11.20	12.30	4.73	6.50	7.46	3.20	7.18	1.85	1.30	5.88
5.62	4.94	15.30	17.70	7.14	5.26	8.09	20.50	10.10	10.30
0.09	0.16	14.40	17.60	4.16	4.53	2.59	15.10	11.10	8.74
1.66	1.60	0.54	0.76	1.08	0.51	1.58	2.14	0.99	5.12
0.29	0.38	0.68	0.80	0.90	1.46	0.58	1.55	1.82	6.14
1.30	1.54	0.84	0.66	1.30	0.47	0.58	0.27	0.38	1.03
2.39	2.96	1.04	1.77	1.35	0.75	1.32	0.36	0.27	0.87
0.51	0.54	0.25	0.27	0.37	0.16	0.31	0.07	0.04	0.26
0.21	0.24	0.26	0.14	0.28	0.66	0.23	0.28	0.42	0.13
2.14	2.39	5.34	6.75	3.22	2.42	2.87	17.74	9.03	17.11
100.98	98.03	101.62	101.25	101.35	101.05	101.42	101.08	101.20	100.87
46.80	50.80	224.00	292.50	238.70	291.00	108.60	100.00	187.90	209.10
229.30	246.90	118.80	156.40	125.20	69.50	116.70	41.40	35.80	95.30
124.70	161.20	61.20	87.80	52.70	30.30	69.90	26.70	14.10	37.50
52.60	55.60	44.30	62.70	50.90	19.00	40.00	29.10	46.60	32.30
23.89	24.93	48.92	75.06	37.51	20.04	39.43	44.38	62.83	33.43
55.00	66.00	29.00	29.00	30.00	26.00	31.00	8.00	7.00	17.00
89.00	89.00	92.00	119.00	<10	26.00	13.00	11.00	20.00	52.00
54.10	97.00	120.40	72.20	55.90	50.40	46.50	60.20	86.00	61.00
11.00	11.00	6.00	8.00	7.00	5.00	7.00	3.00	3.00	4.00
123.00	112.00	124.00	64.00	150.00	65.00	88.00	18.00	15.00	58.00
28.30	32.50	42.60	28.70	50.60	63.70	36.00	23.40	26.40	19.60
9.38	9.10	5.79	4.89	8.43	3.39	6.40	1.28	0.91	5.38
1.62	1.96	2.33	1.42	2.02	2.01	1.63	0.86	0.72	1.38
106.10	114.40	40.10	71.70	49.00	25.50	49.50	11.10	6.00	30.30
4.16	4.85	2.29	3.47	1.75	0.78	1.80	0.32	0.08	0.61
13.37	13.05	6.33	7.36	8.70	4.25	6.71	1.60	0.91	5.06
0.41	0.33	1.18	1.24	0.57	0.62	<0.3	1.33	0.51	1.29
1.20	1.10	0.90	0.70	<0.3	<0.3	<0.3	<0.3	<0.3	<0.3
3.23	3.00	2.99	1.71	3.87	1.59	2.31	0.41	0.37	1.52
0.91	0.89	0.47	0.49	0.80	0.33	0.56	0.10	0.08	0.43
2.50	2.20	1.20	1.10	8.50	2.50	2.10	1.00	<0.8	1.80
1.40	2.80	16.70	13.20	1.20	1.10	1.70	<0.9	<0.9	<0.9
18.40	24.90	84.30	42.30	1.40	2.00	2.00	1.70	1.40	0.90
c	c	c	c	c	c	c	c	c	c
c	c	c	c	c	c	c	c	c	c
31.36	34.32	23.08	18.56	358.00	48.18	30.07	11.65	30.75	16.49
75.57	82.81	61.09	43.42	91.53	102.00	76.39	31.31	29.73	37.26
7.42	8.01	6.40	4.06	9.02	9.38	6.90	3.16	2.80	4.22
28.80	30.30	29.20	16.00	36.90	40.40	26.70	14.50	11.80	17.00
5.95	5.91	7.97	3.85	8.41	10.40	5.68	3.91	2.77	3.78
1.36	1.36	2.00	1.04	2.18	3.48	1.47	1.30	1.09	0.91
5.55	5.73	7.48	4.10	8.54	11.24	5.81	4.11	3.38	3.60
0.80	0.86	1.07	0.63	1.26	1.56	0.86	0.55	0.50	0.53
4.69	4.95	6.08	3.99	7.42	8.64	5.13	3.16	3.22	3.10
0.98	1.08	1.31	0.93	1.58	1.86	1.14	0.70	0.74	0.67
2.38	2.67	3.25	2.60	3.91	4.30	2.85	1.77	1.89	1.69
0.36	0.40	0.51	0.47	0.61	0.58	0.43	0.30	0.29	0.28
2.18	2.46	3.19	3.21	3.70	3.29	2.81	1.98	1.78	1.76
0.34	0.38	0.52	0.56	0.60	0.51	0.46	0.35	0.29	0.28

AGU Geochemistry, Geophysics, Geosystems

10.1002/2015GC005830

Table 4. (continued)

AMK 109 Saluver C Middle Err Piz Nair	AMK 110 Saluver C Middle Err Piz Nair	AMK 111 Saluver C Middle Err Piz Nair	AMK 112 Saluver C Middle Err Piz Nair	AMK 113A Saluver C Middle Err Piz Nair	AMK 113B Saluver C Middle Err Piz Nair	AMK 113C Saluver C Middle Err Piz Nair	AMK 113D Saluver C Middle Err Piz Nair	AMK 113E Saluver C Middle Err Piz Nair	AMK 113F Saluver C Middle Err Piz Nair
87.58	78.48	78.27	55.20	86.70	83.73	82.33	78.62	72.75	60.23
3.83	1.98	3.94	0.80	6.10	6.81	7.44	1.06	2.26	9.92
4.08	4.93	6.61	12.20	3.60	4.41	4.65	4.31	7.62	11.30
1.73	6.43	5.82	22.70	0.19	0.16	0.17	10.20	8.04	4.67
0.90	0.87	0.87	0.35	1.24	1.51	1.61	0.55	0.51	2.24
0.38	0.79	0.80	2.42	0.16	0.23	0.20	0.46	1.97	1.74
0.42	0.47	0.45	0.36	0.62	0.53	0.73	0.20	0.28	1.91
0.78	0.49	1.03	0.34	1.41	1.61	1.66	0.35	0.58	1.42
0.15	0.09	0.14	0.02	0.24	0.25	0.28	0.03	0.08	0.49
0.23	0.15	0.31	0.81	0.16	0.17	0.18	0.14	1.12	0.70
1.61	6.46	3.05	6.64	1.55	1.74	1.75	5.65	3.28	4.59
101.69	101.13	101.29	101.83	101.96	101.15	100.99	101.57	98.49	99.21
79.20	49.10	259.50	821.80	20.30	20.80	24.50	42.80	235.50	204.80
66.90	34.20	81.30	21.90	121.50	129.60	141.30	26.80	47.80	139.90
39.60	19.90	58.20	12.40	88.40	91.40	102.10	22.20	28.10	86.40
15.50	32.80	47.80	27.80	31.30	38.00	41.90	9.80	26.50	69.50
15.43	58.09	55.77	54.46	24.23	25.46	27.46	33.85	30.59	43.00
19.00	18.00	17.00	4.00	30.00	35.00	54.00	12.00	10.00	42.00
20.00	<10	12.00	17.00	<10	17.00	12.00	<10	29.00	54.00
33.70	42.60	42.60	82.20	95.40	353.50	192.80	42.50	53.00	107.50
4.00	3.00	5.00	2.00	6.00	7.00	7.00	2.00	3.00	9.00
38.00	41.00	31.00	7.00	44.00	53.00	47.00	11.00	19.00	108.00
24.20	15.00	30.10	31.80	12.40	14.50	17.80	10.20	55.80	61.20
3.27	2.02	3.01	0.50	5.13	5.19	5.71	0.64	1.67	12.68
0.80	0.59	1.07	2.41	1.14	1.31	1.52	0.35	3.83	2.34
28.40	15.50	37.90	5.10	54.70	62.60	66.00	13.70	23.00	62.50
1.32	0.43	1.28	0.12	1.66	2.31	2.50	0.59	0.85	3.07
3.58	2.09	3.12	0.52	4.70	5.86	4.99	0.73	1.58	12.53
<0.3	<0.3	0.38	1.04	<0.3	<0.3	<0.3	0.37	0.48	0.55
<0.3	<0.3	<0.3	<0.3	<0.3	<0.3	<0.3	<0.3	<0.3	0.80
1.06	1.12	0.83	0.17	1.21	1.43	1.27	0.28	0.49	3.18
0.29	0.19	0.25	0.05	0.39	0.43	0.47	0.06	0.15	1.05
1.40	<0.8	<0.8	<0.8	1.40	1.40	9.20	2.50	1.80	4.90
<0.9	<0.9	<0.9	<0.9	<0.9	<0.9	<0.9	<0.9	<0.9	1.40
0.80	0.90	2.20	0.50	1.50	6.50	2.60	1.30	5.30	6.60
c	c	c	c	c	c	c	c	c	c
c	c	c	c	c	c	c	c	c	c
18.82	12.73	25.58	19.31	17.03	17.70	321.00	50.29	41.33	50.86
45.51	27.46	63.83	37.30	39.60	41.13	47.92	13.25	73.30	136.00
4.84	2.62	5.87	3.17	3.81	4.09	4.86	1.23	5.39	12.70
19.50	10.40	24.00	13.20	14.40	15.60	18.80	4.91	21.00	51.30
4.17	2.22	5.46	2.92	2.79	3.17	3.98	1.09	4.12	11.29
1.12	0.57	1.57	1.20	0.65	0.74	0.93	0.29	1.55	3.01
4.38	2.40	5.95	4.04	2.59	2.91	3.80	1.22	5.68	12.45
0.62	0.36	0.88	0.64	0.36	0.42	0.52	0.20	0.85	1.83
3.69	2.29	4.98	3.95	2.09	2.48	3.00	1.29	5.38	10.40
0.80	0.50	1.01	0.90	0.46	0.53	0.63	0.31	1.34	2.15
1.89	1.28	2.23	2.25	1.12	1.30	1.55	0.86	3.35	4.94
0.29	0.20	0.32	0.34	0.18	0.20	0.23	0.14	0.49	0.72
1.67	1.28	1.85	2.07	1.11	1.21	1.40	0.95	2.73	4.27
0.26	0.21	0.29	0.34	0.17	0.19	0.22	0.15	0.44	0.66

AGU Geochemistry, Geophysics, Geosystems

10.1002/2015GC005830

Table 4. (continued)

RAD. Radiolarite Middle Err Piz Nair	VA-P-5 Saluver A Platta Parsettens	VA-P-6 Saluver A Platta Parsettens	B1-1 Shale Arosa Arosa	B1–2 Shale Arosa Arosa	B2 Shale Arosa Arosa	B6-1 Jaspe Arosa Arosa	B6-2 Jaspe Arosa Arosa	D3 Jaspe Arosa Arosa	D5 Radiolarite Arosa Arosa	D10 Shale Arosa Arosa
87.78	69.40	74.30	69.70	89.00	56.20	68.80	88.90	87.80	83.50	59.10
4.27	15.40	12.70	12.20	4.90	14.30	13.00	4.00	3.30	5.10	16.10
4.68	4.80	3.59	7.00	1.20	11.40	6.30	2.80	3.80	4.30	9.00
0.11	0.05	0.06	<0.001	<0.001	0.13	0.02	0.01	0.01	0.02	0.08
0.78	2.01	1.11	2.91	1.12	8.13	1.95	0.53	0.73	0.81	3.63
0.13	0.19	0.79	0.30	0.11	0.48	0.03	0.02	0.01	0.07	0.57
0.18	1.35	4.15	0.67	0.30	0.68	2.39	1.00	0.28	1.36	2.57
1.36	3.73	1.48	4.41	1.86	2.99	3.44	1.04	0.92	0.92	4.12
0.18	0.64	0.11	0.49	0.20	0.57	0.62	0.15	0.11	0.16	0.60
0.33	0.20	0.16	<0.05	<0.05	0.13	<0.05	<0.05	0.05	<0.05	0.16
0.96	2.88	1.77	2.67	1.11	4.95	3.11	1.62	1.39	1.06	3.07
100.76	97.77	98.45	100.39	99.80	99.96	99.69	100.08	98.40	97.31	99.00
6.80	32.70	19.50	13.00	8.00	18.00	18.00	10.00	8.00	16.00	31.00
115.10	376.40	49.50	133.00	70.00	169.00	206.00	6.00	52.00	83.00	213.00
28.40	73.70	21.50	88.00	229.00	227.00	366.00	106.00	41.00	64.00	128.00
52.50	19.00	53.00	98.00	37.00	488.00	14.00	3.00	38.00	56.00	335.00
18.50	9.00	7.40	28.00	11.00	78.00	9.00	3.00	3.00	5.00	29.00
39.00	63.80	56.40	78.00	65.00	69.00	102.00	49.00	36.00	38.00	63.00
40.00	362.90	105.40	99.00	39.00	129.00	38.00	18.00	32.00	41.00	88.00
20.00	50.20	86.50	<10	33.00	286.00	13.00	<10	28.00	22.00	116.00
<0.07	11.76	4.06	12.00	5.00	14.00	14.00	4.00	5.00	5.00	13.00
51.00	217.50	69.80	104.00	45.00	123.00	134.00	28.00	28.00	36.00	158.00
11.40	37.60	15.00	[c]	[c]	[c]	[c]	[c]	[c]	[c]	[c]
3.70	12.60	6.10	8.41	3.14	11.94	9.22	3.03	2.30	3.18	11.09
0.66	3.45	0.91	1.23	10.09	2.07	1.47	0.80	0.41	0.39	1.78
64.00	146.60	69.80	161.50	65.09	175.63	153.27	51.91	42.35	41.68	159.20
1.80	4.71	1.41	4.67	2.46	9.96	9.32	3.14	1.98	2.45	5.90
3.78	10.87	5.54	[c]	[c]	[c]	[c]	[c]	[c]	[c]	[c]
<0.3	0.70	[c]	[c]	[c]	[c]	[c]	[c]	[c]	[c]	[c]
<0.3	1.10	[c]	[c]	[c]	[c]	[c]	[c]	[c]	[c]	[c]
1.14	5.79	2.54	[c]	[c]	[c]	[c]	[c]	[c]	[c]	[c]
0.25	1.07	1.01	[c]	[c]	[c]	[c]	[c]	[c]	[c]	[c]
1.00	4.30	1.90	[c]	[c]	[c]	[c]	[c]	[c]	[c]	[c]
7.50	[c]	[c]	[c]	[c]	[c]	[c]	[c]	[c]	[c]	[c]
3.30	638.50	148.10	[c]	[c]	[c]	[c]	[c]	[c]	[c]	[c]
0.11	0.30	[c]	[c]	[c]	[c]	[c]	[c]	[c]	[c]	[c]
1.10	7.30	5.80	[c]	[c]	[c]	[c]	[c]	[c]	[c]	[c]
18.00	33.53	6.21	23.57	10.39	42.41	36.00	18.56	9.34	12.33	32.62
37.17	67.47	12.76	59.26	25.64	99.18	72.89	36.92	19.66	27.76	75.92
4.30	7.96	1.61	5.54	2.38	9.66	7.99	4.05	2.11	2.91	7.70
16.28	29.70	5.94	21.14	9.24	34.61	30.31	14.50	7.98	10.36	28.22
3.25	5.98	1.36	4.95	2.19	7.05	5.19	2.28	1.44	1.92	5.96
0.65	1.00	0.15	1.08	0.47	1.46	1.07	0.49	0.25	0.41	1.18
2.71	5.32	1.03	4.11	2.66	6.03	3.74	1.53	1.07	1.67	4.80
0.42	0.81	0.17	0.76	0.47	0.99	0.59	0.21	0.16	0.28	0.78
2.25	4.96	1.81	4.18	2.67	5.54	3.26	1.12	0.89	1.65	4.39
0.46	1.15	0.45	0.84	0.56	1.25	0.78	0.26	0.23	0.45	0.96
1.21	3.06	1.35	2.16	1.38	2.89	2.16	0.72	0.59	1.05	2.24
0.21	0.48	0.26	0.30	0.18	0.52	0.43	0.14	0.12	0.20	0.44
1.19	2.85	1.76	1.77	1.08	3.05	2.66	0.85	0.67	1.24	2.40
0.18	0.42	0.26	0.29	0.16	0.42	0.42	0.14	0.11	0.20	0.39

[a]Major elements (oxides) and LOI are in %wt and trace elements are in ppm.
[b]Results from ICP-AES and the other are from ICP-MS, both analyzed in the LHyGeS-CNRS Strasbourg.
[c]Are elements not analyzed.

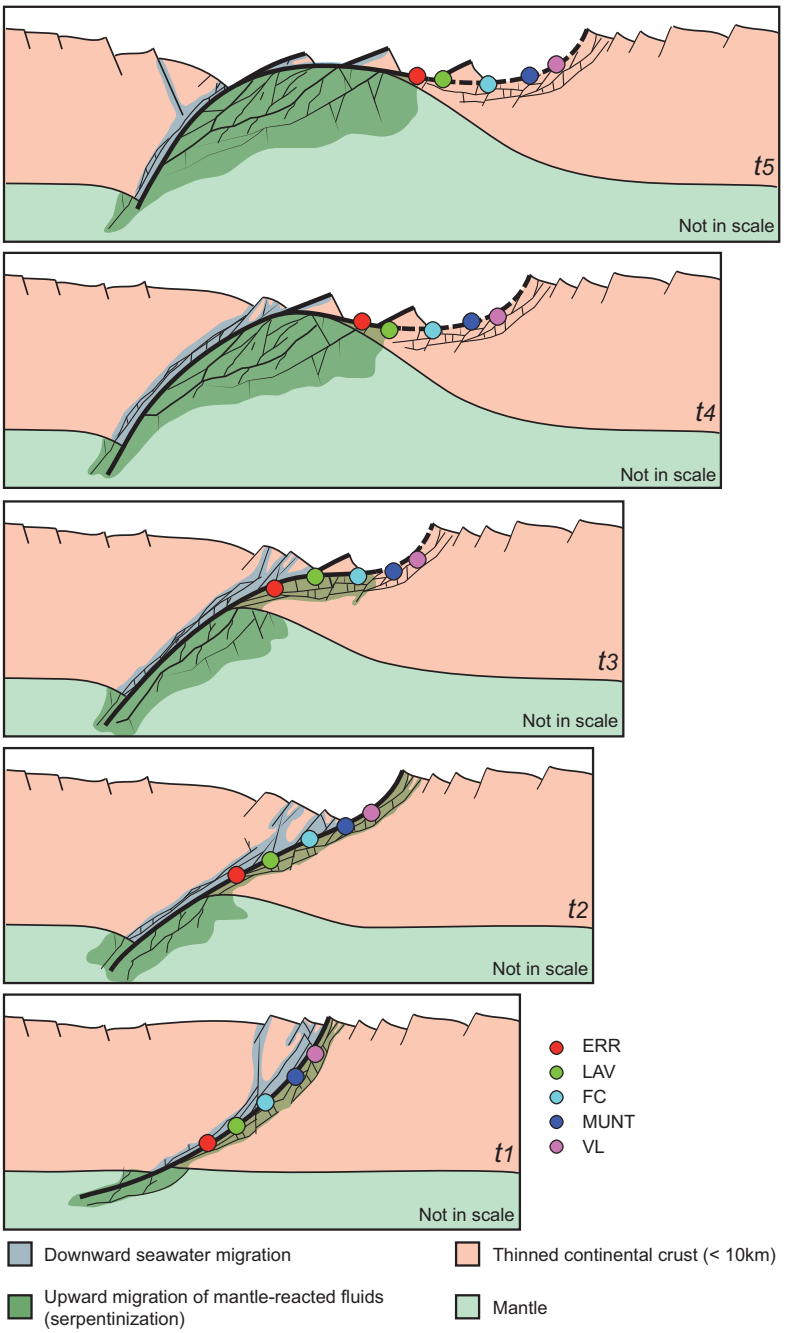

Figure 15. Progressive gain of Ni-Cr-V in different segments of the Err detachment fault. The figures show the concept of the progressive increase of serpentinized area and degree of serpentinization that are linked to the detachment fault evolution. This increase is registered in different segments of the ED (colored dots) according to the results from Figure 10. The light blue zone is the downward migration of the seawater along normal faults in the hanging wall. Seawater reaches the mantle triggering serpentinization producing the mantle-reacted fluids that migrate upward, as illustrated by the dark green zone. In *t1* stage, the deformation is distributed along a high angle normal fault and a set of fractures. From *t2* to *t5*, the deformation is localized along the detachment fault.

depleted in Ni-Cr-V and Fe-Mn compared to the stage registered by the Saluver C. It is worthwhile to mention that the Fe- and Mn-oxides content in the Saluver C is comparable to the hydrothermal mineralization observed in oceanic domains (Figure 13c). Therefore, it can be envisaged that hydrothermal plumes of Fe-Mn escaped through vents spreading over wide areas into the seawater, in a similar way

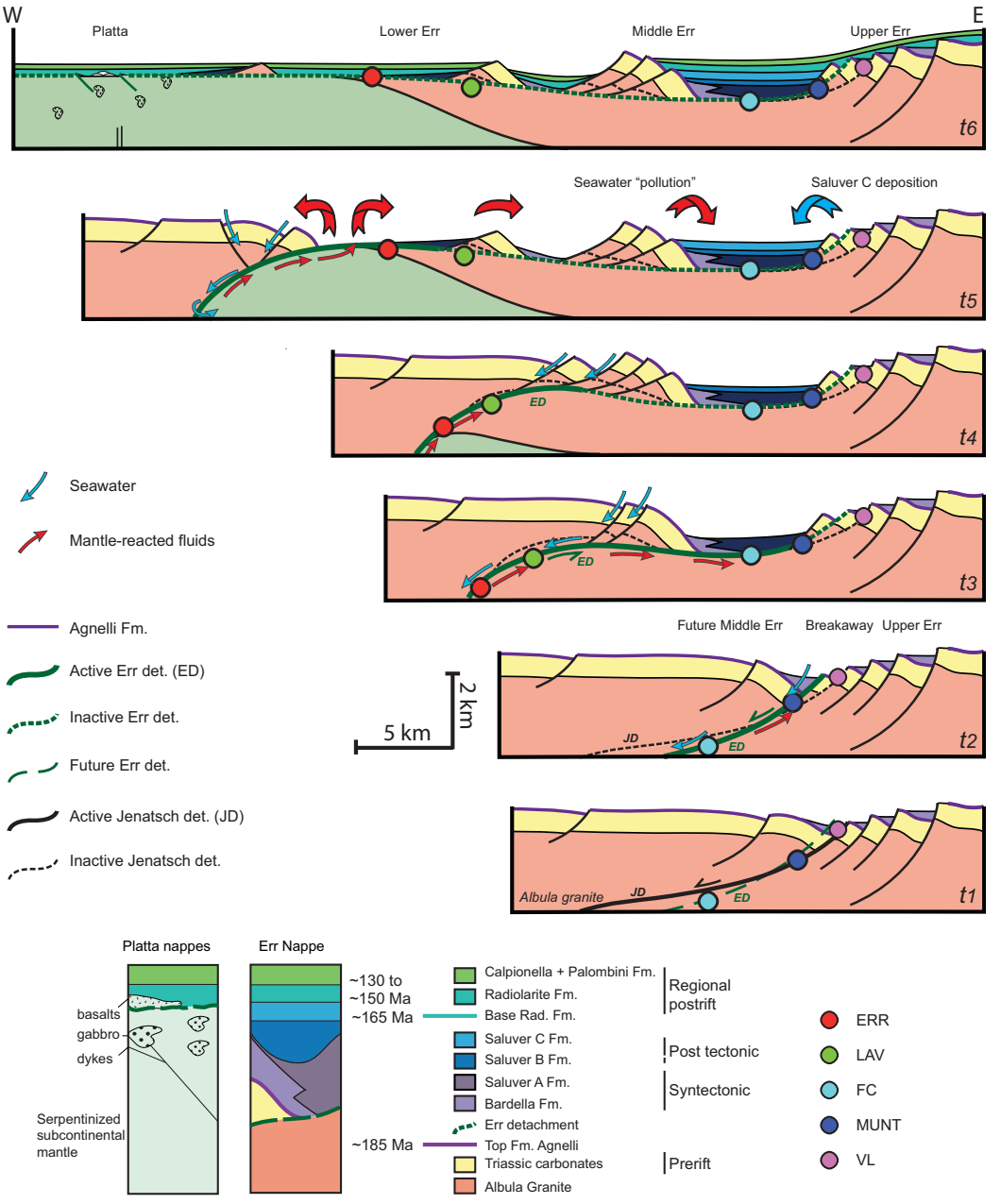

Figure 16. The link between fluid migration and the evolution of supradetachment basins in the Err and Platta nappes. The stage *t1* starts with a listric normal fault system that cuts through the thinned continental crust (<10 km). When the ED becomes active (*t2*), the mantle-reacted fluids migrate along the fault zone toward the overlying syntectonic sediments (*t2* and *t3*). At *t3* the ED became convex up due the upwarping of the footwall along the zone of deformation. When the deformation starts to move toward the future ZECM (from *t4*), the ED segment below the ZoS and Mürtirol become inactive. The continuous deposition of the post tectonic Saluver C (*t5*) records the Seawater Pollution by the rising plume of mantle-reacted fluids. During the deposition of the Radiolarite Formation, the hydrothermal system starts to become less active until a moment that the process stops, as observed by the data from Calpionella and Palombini formations (*t6*). Geological evolution after *Masini et al.* [2012].

to what has been reported in the South Atlantic Ocean (see Figure 1 from *Saito et al.* [2013]). Thus, in contrast to the Ni-Cr-V enrichment in the syntectonic sequence, the observed enrichment of these metals, including Fe and Mn, in the post tectonic sequence may be due to pollution of seawater and their contemporaneous absorption by the clay minerals (Figures 16). The coeval deposited clays in the Saluver C and Radiolarite formations may therefore record the modified seawater signature, similar to clays in present oceanic settings [e.g., *Torfstein*, 2012].

From the Calpionella to the Palombini formations, the system registered a progressive decrease of Ni-Cr-V and Fe-Mn, which values are comparable to those from the Post-Archean Australian Shale (PAAS). This

decrease suggests either the end of the hydrothermal activity or a progressive moving of the source (hydrothermal system) away from the study area. Therefore, the measured Ni-Cr-V and Fe-Mn trends may be used as proxies for mantle exhumation and related serpentinization in hyperextended rifted margins (Figure 16).

7.2. Similarities With Exhumed Mantle at MAR

A number of observations made at MAR favor our interpretation. They are mainly: (1) Ultramafic-hosted hydrothermal fluids expel fluids containing Si, Mg, Fe Ca, Mg, Si, Fe, Mn, and Ni [*Delacour et al*., 2008; *Edmonds*, 2010; *Fouquet et al*., 2010; *Kelley and Shank*, 2010]. This is in agreement with our element loss caused by serpentinization. (2) Fe and Mn oxides are observed in the sedimentary layer around this type of hydrothermal vents [*Dias and Barriga*, 2006]. We also observed an enrichment in the post tectonic Saluver C, which deposition is contemporaneous to mantle exhumation and serpentinization. (3) Late-stage quartz veins are found in oceanic core complexes [*Jöns et al*., 2013]. This shows that Si-rich fluids may be originated during serpentinization evidenced by the occurrence of hydrothermal cherts over the ZECM and the local occurrence of silicified layers in Saluver C over the CDZ. All these observations favor our model in which the enrichment of fluid in elements such as Ni, Cr, V, Si, Fe, and Mn occurs during serpentinization and mantle exhumation under the influence of hydrothermal activity, migrating from the mantle along detachment faults and finally into the sedimentary section. In addition, it supports that elements (especially Ni-Cr-V) can be used as a proxy to trace mantle-reacted fluid along present-day margins.

We are aware that the mobility and solubility/precipitation of these elements can be complex, and usually depend on temperature, salinity, pH and concentration. For example, Cr is assumed to be immobile during serpentinization. However, *Klein-BenDavid et al*. [2011] highlighted that saline hydrous fluids are an important and an efficient agent in Cr mobility in the mantle. In addition, the observed losses of Cr in the orthopyroxene can be one of the explanations for the observed depletion. The detailed analysis of mobility and solubility/precipitation is beyond the scope of this work. But, the fact that these elements are discharged through ultramafic-hosted hydrothermal vents in present-day MAR sites shows that conditions like temperature, pH, and salinity can be favorable for element mobility during serpentinization.

Although fluid inclusions were not investigated, it is well known from MAR studies that serpentinization produces strongly reduced H_2-rich fluids with lower CH_4 content formed under relatively low temperature and higher pH. We think that these gases and conditions probably made part of such mantle-reacted fluids. However, in order to better constrain the conditions at which the fluid-rock reactions took place, more detailed mineralogical and chemical analyses and phase equilibrium modeling would be necessary [e.g., *Destrigneville et al*., 1998].

7.3. Composition of Mantle-Reacted Fluids

It is difficult to reassemble the composition of the mantle-reacted fluids only from chemical analyses of mantle, fault, and sedimentary rocks. However, a first-order composition can be envisaged by the observations that syntectonic phyllosilicates can register partially the fluid flow in the fault rocks and that these fluids also interact with sediments.

As the serpentinization results in fluids enriched in mantle elements, which are found in fault rocks from the ED and in the overlying sediments, and in line with ultramafic-hosted hydrothermal systems at MAR, we conclude that these fluids are composed by Si, Mg, Mn, Fe, Ni, Cr, V, Co, and Sc as well as H_2 and CH_4 gases. As the water-rock interaction involves Jurassic seawater, its chemistry has also to be taken into account.

Although the overall concentration of these elements in the fluid may not be determined, our observations suggest that mantle exhumation and related serpentinization had a significant impact on the chemical budget of the seawater during final rifting in narrow Alpine Tethyan basins.

7.4. Temporal and Spatial Relationships Between Mantle Exhumation, Serpentinization, and the Formation-Migration of the Mantle-Reacted Fluids During the Tectonic Evolution of the Margin

All the aforementioned result allowed us to propose a model of the temporal and spatial distribution of fluids during the evolution of the margin.

As previously discussed (see also Figure 2), the Agnelli formation and the Radiolarite formation constrain the age of the supradetachment basin in the CDZ. This basin was developed in a time interval of

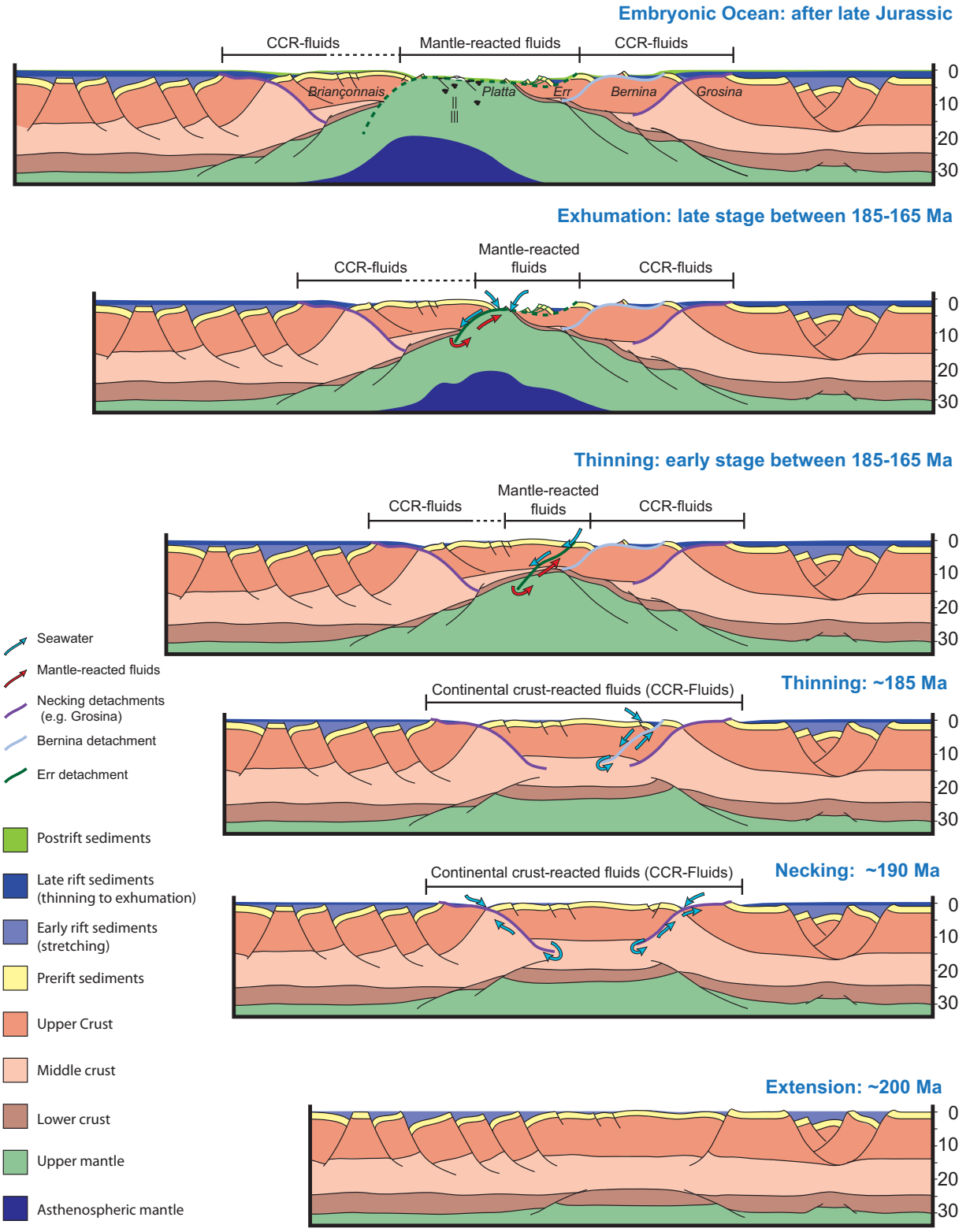

Figure 17. The link between the tectonic evolution and fluid migration along the Alpine Tethyan margin. The Grosina and Bernina detachments record a fluid with a continental composition (about 190–185 Ma). Between 185 and 165 Ma, the ED fault rocks and the supradetachment basin record mantle-reacted fluids that are produced by serpentinization under thinned continental crust. Serpentinization and fluid flow evolve with the progressive mantle exhumation toward the seafloor. During this process, not only the sedimentary basin is affected by fluids but also the sea/ocean reservoir. After late Jurassic, the hydrothermal system at the Platta nappe becomes inactive. Geological evolution after *Mohn et al.* [2011] and *Masini et al.* [2013].

approximately 20 myr, between Pliensbachian and Bathonian. The reworked fault rocks in the sediments show that the ED was also active between 185 and 165 Ma. Because fluid flow is registered in the fault rocks, fluid migration along the ED had to happen during this time interval. The progressive enrichment in Ni-Cr-V registered along the ED and in the syntectonic sediments suggests that this gain had to occur at early stages between 185 and 165 Ma due to the stratigraphic position of the syntectonic sequences and the fault segment of ED (e.g. Alp Muntatsch and Fuorcla Cotschana; for location see Figure 2).

When the segment of the ED under the Zone of Samedan was no longer active and deformation moved oceanward, the fault rocks in this active segment continued to register the increasing serpentinization (e.g., samples from Laviner and Err, Figures 10 and 16). From this moment onward, the post tectonic Saluver C registered an elevated enrichment in Ni-Cr-V and Fe-Mn by the pollution of the seawater that is linked to the ongoing serpentinization and mantle exhumation oceanward. Due to the stratigraphic position of Saluver C, we interpret that this may have happened at a final stage of rifting between 185 and 165 Ma.

It is important to note that the flow of mantle-reacted fluid was not recorded during the formation of the Grosina detachment at about 190Ma and the Bernina detachment at about 185 Ma. It means that these detachments, both older than the ED, may not yet have been connected to the mantle or if they were, serpentinization was not yet significant. However, these detachments record the fluids that interacted with continental rocks what is evidenced by quartz and calcite veins, product of the saussuritization processes along the fault zone.

These observations enable us to outline when and where fluids were active along the evolving Alpine Tethyan margin (Figure 17):

1. Around 190–185Ma: occurrence of first fluid with a signature of the continental crust along the Grosina and Bernina detachments.
2. Early stages between 185 and 165 Ma: serpentinization initiated first under thinned continental crust leading to progressive enrichment of Ni-Cr-V from the breakaway to the end-most segment of ED and resulting in direct migration of mantle-reacted fluids to the sedimentary basin registered in the syntectonic sequences.
3. Late stage between 185 and 165 Ma: important serpentinization stage and mantle exhumation probably accompanied by hydrothermal activity that reached its peak as indicated by the strong enrichment of Ni-Cr-V, Fe, and Mn in the Saluver C.
4. After 165Ma: decreasing influence of the hydrothermal activity in the CDZ as indicated by the decreasing values of Ni-Cr-V and Fe-Mn in the Radiolarite formation and its disappearance in the overlying Calpionella and Palombini formations.

8. Conclusions

In this study, we presented a set of data from the Err and Platta nappes that expose remnants of a CDZ and ZECM that record a large-scale fluid-flow system. The fluid-rock interaction between seawater and mantle leads to serpentinization resulting in the mantle-reacted fluids that is best depicted by enrichment in Ni, Cr, V, Fe, and Mn.

Mantle-reacted fluids migrated through detachment faults and interacted with syn to post tectonic sediments of the distal margin. This is evidenced by the enrichment (gain) of Ni-Cr-V and other elements in the fault and sedimentary rocks, which enables us to trace and date serpentinization, and consequently to understand when and where mantle-reacted fluids circulated in the distal margin. In addition, we suggest that the sedimentary sequence can be used to date the main serpentinization stage and also mantle exhumation in present-day magma-poor rifted margins (e.g., South Atlantic margins).

The determined link between the margin evolution and fluid flow history enables us to establish the importance of the coupling of different reservoirs (mantle, crust, and seawater) during final rifting, which may have a considerable impact on the chemical budget of the seawater and on diagenetic processes during final stages of rifting.

Acknowledgments
Some of the serpentinized peridotite data are from *Müntener et al*. [2010] and part of the ED fault rocks data are from *Manatschal et al*. [2000]. Our sincere thank go to Emmanuel Masini and Geoffroy Mohn for earlier discussions and to Gretchen Früh-Green (ETH-Zurich), Jean-Luc Potdevin (U. Lille), and Philippe Boulvais (Rennes) for fruitful remarks. We appreciate the helpful comments, suggestions, and the review of Nicholas Hayman (UTIG) and the anonymous reviewer. We thank René Boutin and Damien Lemarchand for their help for ICP-MS/AES analyses performed in the LHyGeS at CNRS-Strasbourg University. We are in debt with former master students Martin Stab and Myriam Mahabot from the University of Strasbourg for helping with the analyses of many sedimentary rocks. This research was funded by Petrobras S.A.

References

Ague, J. J., J. L. M. van Haren (1996), Assessing metasomatic mass and volume changes using the bootstrap, with application to deep crustal hydrothermal alteration of marble, *Econ. Geol.*, *91*(7), 1169–1182, doi:10.2113/gsecongeo.91.7.1169.

Baumgartner, P. O. (1987), Age and genesis of Tethyan Jurassic Radiolarites, *Eclogae Geol. Helv.*, *80*(3), 831–879.

Bernoulli, D., and H. Weissert (1985), Sedimentary fabrics in Alpine ophicalcites, south Pennine Arosa zone, Switzerland, *Geology*, *13*, 755–758, doi:10.1130/0091-7613(1985)13<755:SFIAOS>2.0.CO;2.

Bill, M., L. O'Dogherty, J. Guex, P. O. Baumgartner, and H. Masson (2001), Radiolarite ages in Alpine-Mediterranean ophiolites: Constraints on the oceanic spreading and the Tethys-Atlantic connection, *Bull. Geol. Soc. Am.*, *113*(1), 129–143, doi:10.1130/0016-7606(2001)113<0129:RAIAMO>2.0.CO;2.

Bons, P. D., M. A. Elburg, and E. Gomez-Rivas (2012), A review of the formation of tectonic veins and their microstructures, *J. Struct. Geol.*, *43*, 33–62, doi:10.1016/j.jsg.2012.07.005.

Bracciali, L., M. Marroni, P. Luca, and R. Sergio (2007), Geochemistry and petrography of Western Tethys Cretaceous sedimentary covers (Corsica and Northern Apennines): From source areas to configuration of margins, *Geol. Soc. Am. Spec. Pap.*, *420*, 73–93, doi:10.1130/2006.2420(06).

Bracciali, L., L. Pandolfi, and S. Rocchi (2013), A snapshot of the Late Jurassic Western Tethys seafloor composition and morphology provided by the geochemistry of pelitic sediments (Corsica, Central Alps and Northern Apennines), *Basin Res.*, *25*, 1–25, doi:10.1111/bre.12036.

Buatier, M. D., G. L. Früh-Green, and A. M. Karpoff (1995), Mechanisms of Mg-phyllosilicate formation in a hydrothermal system at a sedimented ridge (Middle Valley, Juan de Fuca), *Contrib. Mineral. Petrol.*, *122*(1–2), 134–151, doi:10.1007/s004100050117.

Condie, K. C. (1993), Chemical composition and evolution of the upper continental crust: Contrasting results from surface samples and shales, *Chem. Geol.*, *104*(1–4), 1–37, doi:10.1016/0009-2541(93)90140-E.

Cordey, F., and A. Bailly (2007), Alpine ocean seafloor spreading and onset of pelagic sedimentation: New radiolarian data from the Chenaillet-Montgenèvre ophiolite (French-Italian Alps), *Geodin. Acta*, *20*(3), 131–138, doi:10.3166/ga.20.131-138.

Cornelius, H. P. (1932), Geologische Karte der Err-Julier-Gruppe 1:25000, *Schweiz Geol Komm Spez.*, *115A*.

Dean, S., and T. Minshull (2000), Deep structure of the ocean-continent transition in the southern Iberia Abyssal Plain from seismic refraction profiles: The IAM-9 transect at 40°20′ N, *J. Geophys. Res.*, *105*(B3), 5859–5885, doi:10.1029/1999JB900301.

Delacour, A., G. L. Früh-Green, S. M. Bernasconi, P. Schaeffer, and D. S. Kelley (2008), Carbon geochemistry of serpentinites in the Lost City Hydrothermal System (30°N, MAR), *Geochim. Cosmochim. Acta*, *72*(15), 3681–3702, doi:10.1016/j.gca.2008.04.039.

deMartin, B. J., R. A. Sohn, J. Pablo Canales, and S. E. Humphris (2007), Kinematics and geometry of active detachment faulting beneath the Trans-Atlantic Geotraverse (TAG) hydrothermal field on the Mid-Atlantic Ridge, *Geology*, *35*(8), 711, doi:10.1130/G23718A.1.

Desmurs, L., G. Manatschal, and D. Bernoulli (2001), The Steinmann Trinity revisited: Mantle exhumation and magmatism along an ocean-continent transition: The Platta nappe, eastern Switzerland, *Geol. Soc. Spec. Publ.*, *187*(1), 235–266, doi:10.1144/GSL.SP.2001.187.01.12.

Destrigneville, C., A. M. Karpoff, and D. Charpentier (1998) Modelling the halmyrolytic formation of palygorskite from serpentinite, in *Water-Rock Interaction-WRI9th Proceedings*, edited by G. Arehart and J. Hulston, pp. 715–718, A. A. Balkema.

Destrigneville, C., A. Karpoff, and D. Charpentier (1998), 'Modelling the halmyrolytic formation of palygorskite from serpentinite' 'Water-Rock Interaction: Proceedings of the 9th International Symposium on Water-Rock Interaction–Wri-9, Taupo, New Zealand, 30 March–3 April', AA Balkema.

Dewit, J., A. Foubert, H. A. El Desouky, P. Muchez, D. Hunt, and R. Swennen (2012), Dolomitisation model of hydrothermal dolomites (HTD) hosted by Aptian-Albian carbonates of the Ramales platform (Basque-Cantabrian basin, northern Spain), in *GEOFLUIDS VII: International Conference*, pp. 75–78, Paris, France.

Dias, Á. S., and F. J. A. S. Barriga (2006), Mineralogy and geochemistry of hydrothermal sediments from the serpentinite-hosted Saldanha hydrothermal field (36°34′N; 33°26′W) at MAR, *Mar. Geol.*, *225*(1–4), 157–175, doi:10.1016/j.margeo.2005.07.013.

Dias, Á. S., G. L. Früh-Green, S. M. Bernasconi, and F. J. A. S. Barriga (2011), Geochemistry and stable isotope constraints on high-temperature activity from sediment cores of the Saldanha hydrothermal field, *Mar. Geol.*, *279*(1–4), 128–140, doi:10.1016/j.margeo.2010.10.017.

Dommergues, J.-L., C. Meister, and G. Manatschal (2012), Early Jurassic ammonites from Bivio (Lower Austroalpine unit) and Ardez (Middle Penninic unit) areas: A biostratigraphic tool to date the rifting in the Eastern Swiss Alps, *Rev. Paléobiol. Genève*, *11*, 43–52.

Douville, E., J. L. Charlou, E. H. Oelkers, P. Bienvenu, C. F. J. Colon, J. P. Donval, Y. Fouquet, D. Prieur, and P. Appriou (2002), The Rainbow vent fluids (36°14′N, MAR): The influence of ultramafic rocks and phase separation on trace metal content in Mid-Atlantic Ridge hydrothermal fluids, *Chem. Geol.*, *184*, 37–48, doi:10.1016/S0009-2541(01)00351-5.

Eberli, G. (1988), The evolution of the southern continental margin of the Jurassic Tethys Ocean as recorded in the Allgäu Formation of the Austroalpine Nappes of Graubünden (Switzerland), *Eclogae Geol. Helv.*, *81*(1), 175–214.

Edmonds, H. N. (2010), Chemical signatures from hydrothermal venting on slow spreading ridges, in *Diversity of Hydrothermal Systems on Slow Spreading Ocean Ridges*, vol. 188, edited by P. A. Rona et al., pp. 27–42, AGU, Washington, D. C.

Engström, A., A. Skelton, and N. Grassineau (2007), Isotopic and petrological evidence of fluid-rock interaction at a Tethyan ocean-continent transition in the Alps: Implications for tectonic processes and carbon transfer during early ocean formation, *Geofluids*, *7*(4), 401–414, doi:10.1111/j.1468-8123.2007.00194.x.

Evans, J. P., C. B. Forster, and J. V. Goddard (1997), Permeability of fault-related rocks, and implications for hydraulic structure of fault zones, *J. Struct. Geol.*, *19*(11), 1393–1404, doi:10.1016/S0191-8141(97)00057-6.

Evans, B. W., K. Hattori, and A. Baronnet (2013), Serpentinite: What, Why, Where?, *Elements*, *9*(2), 99–106, doi:10.2113/gselements.9.2.99.

Ferreiro Mählmann, R. (1996), The pattern of diagenesis and metamorphism by vitrinite reflectance and illite "crystallinity" in Mittelbünden and in the Oberhalbstein: Part 2: Correlation of coal petrographical and of mineralogical parameters, *Schweiz. Mineral. Petrogr. Mitt.*, *76*, 23–46.

Finger, W. (1978), Die Zone von Samaden (unterostalpine Decken, Graubünden) und ihre jurassischen Brekzien, PhD thesis, ETH Zürich, Zurich, doi:10.3929/ethz-a-000164017.

Fouquet, Y., et al. (2010), Geodiversity of hydrothermal processes along the Mid-Atlantic Ridge and ultramafic-hosted mineralization: A new type of oceanic Cu-Zn-Co-Au volcanogenic massive sulfide deposit, in *Diversity of Hydrothermal Systems on Slow Spreading Ocean Ridges*, vol. 188, edited by P. A. Rona et al.,pp. 321–367, AGU, Washington, D. C., doi:10.1029/2008GM000746.

Froitzheim, N., and G. P. Eberli (1990), Extensional detachment faulting in the evolution of a Tethys passive continental margin, Eastern Alps, Switzerland, *Geol. Soc. Am. Bull.*, *102*(9), 1297–1308.

Froitzheim, N., and G. Manatschal (1996), Kinematics of Jurassic rifting, mantle exhumation, and passive-margin formation in the Austroalpine and Penninic nappes (eastern Switzerland), *Geol. Soc. Am. Bull.*, *108*(9), 1120–1133.

Früh-Green, G. L., H. Weissert, and D. Bernoulli (1990), A multiple fluid history recorded in Alpine ophiolites, *J. Geol. Soc. London*, *147*, 959–970, doi:10.1144/gsjgs.147.6.0959.
Govindaraju, K. (1995), 1995 working values with confidence limits for twenty-six CRPG, ANRT and IWG-GIT geostandards, *Geostand. Newsl.*, *19*, 1–32, doi:10.1111/j.1751-908X.1995.tb00164.x.
Grant, J. A. (1986), The isocon diagram; a simple solution to Gresens' equation for metasomatic alteration, *Econ. Geol.*, *81*(8), 1976–1982, doi:10.2113/gsecongeo.81.8.1976.
Gresens, R. (1967), Composition-volume relationships of metasomatism, *Chem. Geol.*, *2*, 47–65.
Hayman, N. W. (2006), Shallow crustal fault rocks from the Black Mountain detachments, Death Valley, CA, *J. Struct. Geol.*, *28*(10), 1767–1784, doi:10.1016/j.jsg.2006.06.017.
Jin, Z., L. Zhang, L. Yang, and W. Hu (2004), A preliminary study of mantle-derived fluids and their effects on oil/gas generation in sedimentary basins, *J. Pet. Sci. Eng.*, *41*(1–3), 45–55, doi:10.1016/S0920-4105(03)00142-6.
Jöns, N., W. Bach, M. Rosner, and B. Plessen (2013), Formation of late-stage mineral veins in the footwall of an oceanic detachment fault (ODP Leg 304/305), *Geophys. Res. Abstr.*, *15*, EGU2013–5457.
Karpoff, A. M., A.-V. Walter, and C. Pflumio (1988), Metalliferous sediments within lava sequences of the Sumail ophiolite (Oman): Mineralogical and geochemical characterization, origin and evolution, *Tectonophysics*, *151*(1–4), 223–245, doi:10.1016/0040-1951(88)90247-8.
Kelley, D. S., and T. M. Shank (2010), Hydrothermal systems: A decade of discovery in slow spreading environments, in *Diversity of Hydrothermal Systems on Slow Spreading Ocean Ridges*, edited by P. A. Rona, vol. 188, pp. 369–407, AGU, Washington, D. C.
Kelley, D. S., et al. (2001), An off-axis hydrothermal vent field near the Mid-Atlantic Ridge at 30 degrees N., *Nature*, *412*(6843), 145–149, doi:10.1038/35084000.
Klein, F., W. Bach, S. E. Humphris, W.-A. Kahl, N. Jons, B. Moskowitz, and T. S. Berquo (2013), Magnetite in seafloor serpentinite: Some like it hot, *Geology*, *42*(2), 135–138, doi:10.1130/G35068.1.
Klein-BenDavid, O., T. Pettke, and R. Kessel (2011), Chromium mobility in hydrous fluids at upper mantle conditions, *Lithos*, *125*(1–2), 122–130, doi:10.1016/j.lithos.2011.02.002.
Klemme, S. (2004), The influence of Cr on the garnet–spinel transition in the Earth's mantle: Experiments in the system MgO–Cr_2O_3–SiO_2 and thermodynamic modelling, *Lithos*, *77*(1–4), 639–646, doi:10.1016/j.lithos.2004.03.017.
Kelemen, P. B., and G. Hirth (2012), Reaction-driven cracking during retrograde metamorphism: Olivine hydration and carbonation, *Earth Planet. Sci. Lett.*, *345–348*, 81–89, doi:10.1016/j.epsl.2012.06.018.
Lemoine, M., and R. Trümpy (1987), Pre-oceanic rifting in the Alps, *Tectonophysics*, *133*, 305–320.
Lemoine, M., T. Bas, M. Bourbon, P.-C. Graciansky, J.-L. Rudkiewicz, J. Megard-Galli, and P. Tricart (1986), The continental margin of the Mesozoic Tethys in the Western Alps, *Mar. Pet. Geol.*, *3*, 179–199.
López-Horgue, M. A., E. Iriarte, S. Schröder, P. A. Fernández-Mendiola, B. Caline, H. Corneyllie, J. Frémont, M. Sudrie, and S. Zerti (2010), Structurally controlled hydrothermal dolomites in Albian carbonates of the Asón valley, Basque Cantabrian Basin, Northern Spain, *Mar. Pet. Geol.*, *27*(5), 1069–1092, doi:10.1016/j.marpetgeo.2009.10.015.
MacLean, W. H., and T. J. Barrett (1993), Lithogeochemical techniques using immobile elements, *J. Geochem. Explor.*, *48*(2), 109–133, doi:10.1016/0375-6742(93)90002-4.
Manatschal, G. (1995), Jurassic rifting and formation of a passive continental margin (Platta and Err nappes, Eastern Switzerland): Geometry, kinematics and geochemestry of fault rocks and a comparision with the Galicia margin, PhD thesis, ETH Zürich, Zurich. [Available at http://dx.doi.org/10.3929/ethz-a-001533748.]
Manatschal, G. (1999), Fluid-and reaction-assisted low-angle normal faulting: Evidence from rift-related brittle fault rocks in the Alps (Err Nappe, eastern Switzerland), *J. Struct. Geol.*, *21*(7), 777–793.
Manatschal, G. (2004), New models for evolution of magma-poor rifted margins based on a review of data and concepts from West Iberia and the Alps, *Int. J. Earth Sci.*, *93*(3), 1–35. doi:10.1007/s00531-004-0394-7.
Manatschal, G., and O. Müntener (2009), A type sequence across an ancient magma-poor ocean–continent transition: The example of the western Alpine Tethys ophiolites, *Tectonophysics*, *473*(1–2), 4–19, doi:10.1016/j.tecto.2008.07.021.
Manatschal, G., and P. Nievergelt (1997), A continent-ocean transition recorded in the Err and Platta nappes (Eastern Switzerland), *Eclogae Geol. Helv.*, *90*(1), 3–27.
Manatschal, G., D. Marquer, and G. L. Früh-Green (2000), Channelized fluid flow and mass transfer along a rift-related detachment fault (Eastern Alps, southeast Switzerland), *Geol. Soc. Am. Bull.*, *112*(1), 21. doi:10.1130/0016-7606(2000)112<21:CFFAMT>2.0.CO;2.
Manatschal, G., N. Froitzheim, M. Rubenach, and B. D. Turrin (2001), The role of detachment faulting in the formation of an ocean-continent transition: Insights from the Iberia Abyssal Plain, *Geol. Soc. Spec. Publ.*, *187*(1), 405–428.
Marroni, M., L. Pandolfi, and N. Perilli (2000), Calcareous nannofossil dating of the San Martino formation from the Balagne ophiolite sequence (alpine Corsica): Comparison with the Palombini shale of the northern Apennine, *Ofioliti*, *25*(2), 147–155.
Masini, E., G. Manatschal, G. Mohn, J. Ghienne, and F. Lafont (2011), The tectono-sedimentary evolution of a supra-detachment rift basin at a deep-water magma-poor rifted margin: The example of the Samedan Basin preserved in the Err nappe in SE Switzerland, *Basin Res.*, *23*(6), 652–677, doi:10.1111/j.1365-2117.2011.00509.x.
Masini, E., G. Manatschal, G. Mohn, and P. Unternehr (2012), Anatomy and tectono-sedimentary evolution of a rift-related detachment system: The example of the Err detachment (central Alps, SE Switzerland), *Geol. Soc. Am. Bull.*, *124*(9–10), 1535–1551, doi:10.1130/B30557.1.
Masini, E., G. Manatschal, and G. Mohn (2013), The Alpine Tethys rifted margins: Reconciling old and new ideas to understand the stratigraphic architecture of magma-poor rifted margins, edited by H. Weissert, *Sedimentology*, *60*(1), 174–196, doi:10.1111/sed.12017.
McKenzie, J., A. Isern, A. M. Karpoff, and P. Swart (1990), Basal dolomitic sediments, Tyrrhenian sea, ODP Leg 107, in *Proceedings of Ocean Drilling Program Science Results*, vol. 107, edited by K. A. Kastens et al., pp. 141–152, Ocean Drill. Program, College Station, Tex., doi:10.2973/odp.proc.sr.107.124.1990.
Miller, D. J., and N. I. Christensen (1997), Seismic velocities of lower crustal and upper mantle rocks from the slow-spreading Mid-Atlantic ridge south of the Kane transform zone (MARK), in *Proceedings of Ocean Drilling Program Science Results*, vol. 153, edited by J. A. Karson et al., pp. 437–454, Ocean Drill. Program, College Station, Tex.
Mitchell, T. M., and D. R. Faulkner (2012), Towards quantifying the matrix permeability of fault damage zones in low porosity rocks, *Earth Planet. Sci. Lett.*, *339–340*, 24–31, doi:10.1016/j.epsl.2012.05.014.
Mohn, G., G. Manatschal, O. Müntener, M. Beltrando, and E. Masini (2010), Unravelling the interaction between tectonic and sedimentary processes during lithospheric thinning in the Alpine Tethys margins, *Int. J. Earth Sci.*, *99*, 75–101, doi:10.1007/s00531-010-0566-6.
Mohn, G., G. Manatschal, and E. Masini (2011), Rift-related inheritance in orogens: A case study from the Austroalpine nappes in Central Alps (SE-Switzerland and N-Italy), *J. Earth Sci.*, *100*(5), 937–961, doi:10.1007/s00531-010-0630-2.

Mohn, G., G. Manatschal, M. Beltrando, E. Masini, and N. Kusznir (2012), Necking of continental crust in magma-poor rifted margins: Evidence from the fossil Alpine Tethys margins, *Tectonics*, *31*, TC1012, doi:10.1029/2011TC002961.
Moody, J. B. (1976), Serpentinization: A review, *Lithos*, *9*(2), 125–138, doi:10.1016/0024-4937(76)90030-X.
Morrow, C. A., L. Q. Shi, and J. D. Byerlee (1984), Permeability of fault gouge under confining pressure and shear stress, *J. Geophys. Res.*, *89*(B5), 3193–3200, doi:10.1029/JB089iB05p03193.
Müntener, O., J. Hermann, and V. Trommsdorff (2000), Cooling history and exhumation of lower-crustal granulite and upper mantle (Malenco, eastern Central Alps), *J. Petrol.*, *41*(2), 175–200, doi:10.1093/petrology/41.2.175.
Müntener, O., G. Manatschal, L. Desmurs, and T. Pettke (2010), Plagioclase peridotites in ocean-continent transitions: Refertilized mantle domains generated by melt stagnation in the Shallow mantle lithosphere, *J. Petrol.*, *51*(1–2), 255–294, doi:10.1093/petrology/egp087.
Ogasawara, Y., A. Okamoto, N. Hirano, and N. Tsuchiya (2013), Coupled reactions and silica diffusion during serpentinization, *Geochim. Cosmochim. Acta*, *119*, 212–230, doi:10.1016/j.gca.2013.06.001.
Péron-Pinvidic, G., and G. Manatschal (2009), The final rifting evolution at deep magma-poor passive margins from Iberia-Newfoundland: A new point of view, *Int. J. Earth Sci.*, *98*(7), 1581–1597.
Perseil, E. A., and L. Latouche (1989), Découverte de microstructures de nodules polymétaliques dans les minéralisations manganésifères métamorphiques de Falotta et de Parsettens (Grisons-Suisse), *Miner. Deposita*, *24*, 111–116.
Peters, T., and A. Stettler (1987), Radiometric age, thermobarometry and mode of emplacement of the Totalp periodite in the Eastern Swiss Alps, *Schweiz. Mineral. Petrogr. Mitt.*, *67*(3), 285–294.
Picazo, S. (2012), *Déformation des roches ultramafiques liée à l'exhumation dans les dorsales et les transitions océan continent*, PhD thesis, 258 pp., Inst. de Phys. du Globe, Paris.
Picazo, S., G. Manatschal, M. Cannat, and M. Andréani (2013), Deformation associated to exhumation of serpentinized mantle rocks in a fossil Ocean Continent Transition: The Totalp unit in SE Switzerland, *Lithos*, *175–176*, 255–271, doi:10.1016/j.lithos.2013.05.010.
Potdevin, J. L., and D. Marquer (1987), Quantitative methods for the estimation of mass transfers by fluids in deformed metamorphic rocks, *Geodin. Acta*, *1*(3), 193–206.
Reston, T. J., and C. R. Ranero (2011), The 3-D geometry of detachment faulting at mid-ocean ridges, *Geochem. Geophys. Geosyst.*, *12*, Q0AG05, doi:10.1029/2011GC003666.
Rouméjon S., and M. Cannat (2014), Serpentinization of mantle-derived peridotites at mid-ocean ridges: Mesh texture development in the context of tectonic exhumation, *Geochem.Geophys. Geosyst.*, *15*, 2354–2379, doi:10.1002/2013GC005148.
Saito, M. A., A. E. Noble, A. Tagliabue, T. J. Goepfert, C. H. Lamborg, and W. J. Jenkins (2013), Slow-spreading submarine ridges in the South Atlantic as a significant oceanic iron source, *Nat. Geosci.*, *6*(9), 775–779, doi:10.1038/ngeo1893.
Santos Neto, E. V., J. R. Cerqueira, and A. Prinzhofer (2011), Natural gas geochemistry of the southern offshore Brazilian Basins, in *International Meeting on Organic Geochemistry*, p. 264.
Schaltegger, U., L. Desmurs, G. Manatschal, O. Muntener, M. Meier, M. Frank, and D. Bernoulli (2002), The transition from rifting to sea-floor spreading within a magma-poor rifted margin: Field and isotopic constraints, *Terra Nova*, *14*, 156–162.
Schmid, S. M., B. F. Genschuh, E. Kissling, R. Schuster, and B. Fugenschuh (2004), Tectonic map and overall architecture of the Alpine orogen, *Eclogae Geol. Helv.*, *97*(1), 93–117.
Schuiling, R. D. (1964), Serpentinization as a possible cause of high heat-flow values in and near the oceanic ridges, *Nature*, *201*(4921), 807–808, doi:10.1038/201807b0.
Stipp, M., H. Stünitz, R. Heilbronner, and S. Schmid (2002), The eastern Tonale fault zone: A "natural laboratory" for crystal plastic deformation of quartz over a temperature range from 250 to 700°C, *J. Struct. Geol.*, *24*(12), 1861–1884, doi:10.1016/S0191-8141(02)00035-4.
Sutra, E., and G. Manatschal (2012), How does the continental crust thin in a hyperextended rifted margin? Insights from the Iberia margin, *Geology*, 40(2), 139–142, doi:10.1130/G32786.1.
Szatmari, P., T. C. O. Fonseca, and N. F. Miekeley (2011), Mantle-like trace element composition of petroleum: Contributions from serpentinizing peridotites, in *Tectonics*, chap.13, edited by D. Closson, pp. 1–28, InTech, doi:10.5772/14063. [Available at http://www.intechopen.com/books/tectonics/mantle-like-trace-element-composition-of-petroleum-contributions-from-serpentinizing-peridotites.]
Tenthorey, E., and J. Fitzgerald (2006), Feedbacks between deformation, hydrothermal reaction and permeability evolution in the crust: Experimental insights, *Earth Planet. Sci. Lett.*, *247*(1–2), 117–129, doi:10.1016/j.epsl.2006.05.005.
Torfstein, A. (2012), Size fractionation, reproducibility and provenance of helium isotopes in north-equatorial pacific pelagic clays, *Earth Planet. Sci. Lett.*, *339–340*, 151–163, doi:10.1016/j.epsl.2012.05.030.
Trommsdorff, V., and B. W. Evans (1974), Alpine metamorphism of peridotitic rocks, *Schweiz. Mineral. Petrogr. Mitt.*, *54*, 333–354.
Trümpy, R. (1975), Penninic-Austroalpine boundary in the Swiss Alps: A presumed former continental margin and its problems, *Am. J. Sci.*, *275-A*, 209–238.
Whitney, D. L., C. Teyssier, P. Rey, and W. R. Buck (2013), Continental and oceanic core complexes, *Geol. Soc. Am. Bull.*, *125*(3–4), 273–298, doi:10.1130/B30754.1.